NASA-CR-159849

NASA CR - 159849

ION EXTRACTION FROM A PLASMA

PREPARED FOR

LEWIS RESEARCH CENTER

NATIONAL AERONAUTICS AND SPACE ADMINISTRATION

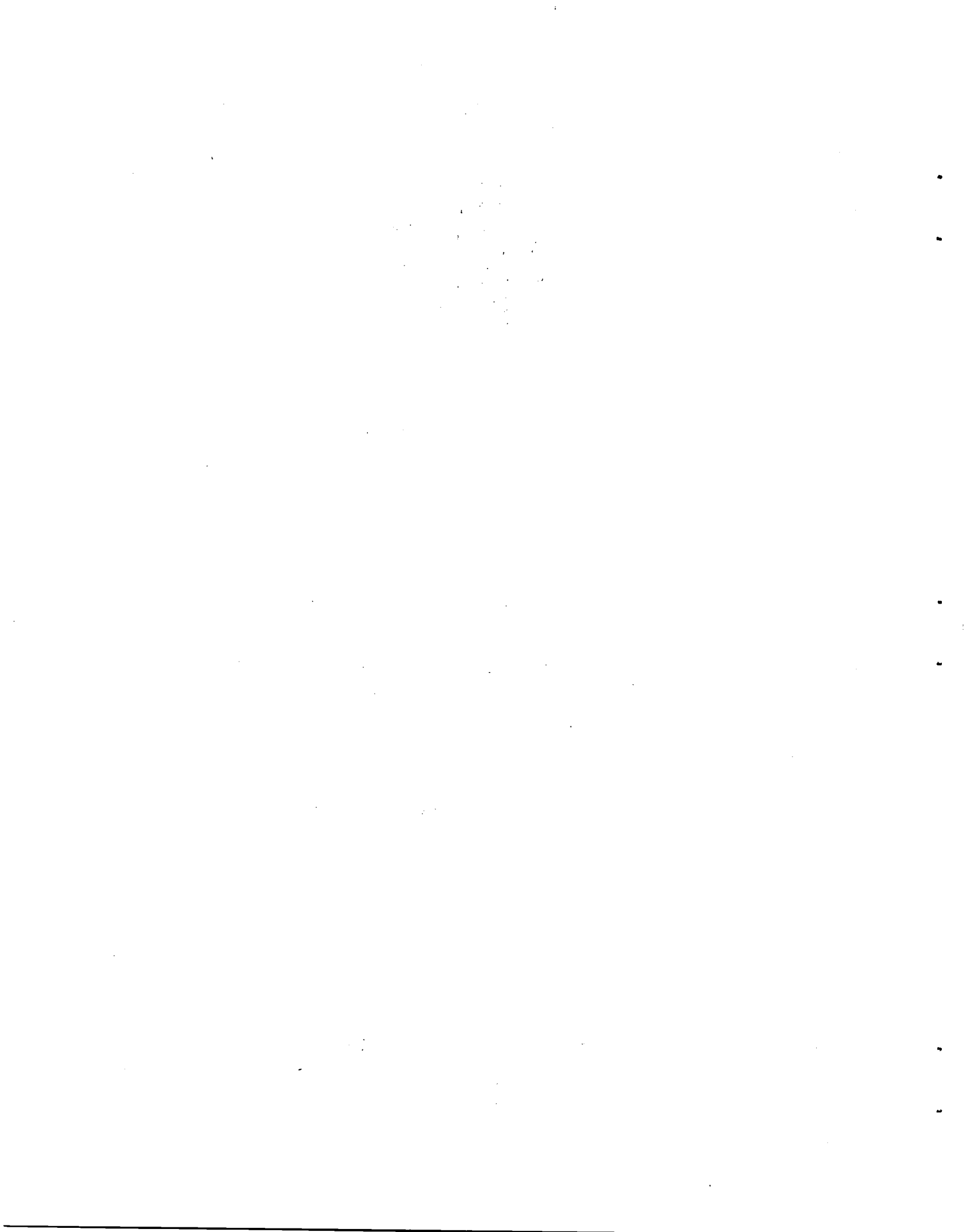Grant NGR-06-002-112

by

Graeme Aston

Approved by

Paul J. Wilbur

June 1980

Department of Mechanical Engineering
Colorado State University
Fort Collins, Colorado

1. Report No. NASA CR 159849	2. Government Accession No.	3. Recipient's Catalog No.
4. Title and Subtitle Ion Extraction from a Plasma		5. Report Date June 1980
		6. Performing Organization Code
7. Author(s) Graeme Aston and Paul J. Wilbur		8. Performing Organization Report No.
		10. Work Unit No.
9. Performing Organization Name and Address Department of Mechanical Engineering Colorado State University Fort Collins, Colorado 80523		11. Contract or Grant No. NGR-06-002-112
		13. Type of Report and Period Covered
12. Sponsoring Agency Name and Address National Aeronautics and Space Administration Washington, D.C. 20546		Dec. 1, 1979 - Dec. 1, 1980
		14. Sponsoring Agency Code

15. Supplementary Notes Grant Monitor - William Kerslake, NASA Lewis Research Center, Cleveland, Ohio 44135. This report is a reproduction of the Ph.D. dissertation of Dr. Graeme Aston. It is submitted to the sponsor and to the distribution list in this form both as a presentation of the technical material, and as an indication of the academic program supported by the grant.

16. Abstract

An experimental investigation of the physical processes governing ion extraction from a plasma is presented. The screen hole plasma sheath of a multi-aperture ion accelerator system is defined by equipotential plots for a variety of accelerator system geometries and operating conditions. A sheath thickness of at least fifteen Debye lengths is shown to be typical. The electron density variation within the sheath satisfies a Maxwell-Boltzmann density distribution at an effective electron temperature dependent on the discharge plasma primary-to-Maxwellian electron density ratio. Plasma ion flow up to and through the sheath is predominately one dimensional and the ions enter the sheath with a modified Bohm velocity. Low values of the screen grid thickness to screen hole diameter ratio give good ion focusing and high extracted ion currents because of the effect of screen webbing on ion focusing.

17. Key Words (Suggested by Author(s)) Electrostatic Acceleration	18. Distribution Statement Unclassified - Unlimited

19. Security Classif. (of this report) Unclassified	20. Security Classif. (of this page) Unclassified	21. No. of Pages 92	22. Price*

N80-26161#

TABLE OF CONTENTS

TABLE OF FIGURES

Table of Figures (Cont.)   <u>Page</u>

INTRODUCTION

The ion beam divergence characteristics of ion accelerator systems have been studied by many workers in recent years.[1-7] This increased interest in ion-optical phenomena is a result of the direct application of ion beams to three new technology areas that have evolved rapidly in the last decade. Briefly, these areas are the following. Electric propulsion of space vehicles; where ion thrusters provide thrust by ejecting beams of energetic ions. Neutral beam heating of fusion plasmas; where deuterium ions are accelerated, resonant charge exchanged, and injected into a fusion device as neutral particles to heat directly the confined plasma. Ion beam sputtering, deposition and milling; where carefully controlled ion fluxes are used to alter the surface structure and/or composition of thin films for semi-conductor and other applications. Well focused, high current, ion beams are a necessary requirement in each of the aforementioned areas.

Presently, the ion acceleration and focusing process is fairly well understood. Using the data available in Refs. 6 and 7, one can quite accurately predict the ion beam divergence characteristics of an arbitrary two or three-grid ion accelerator system design over a wide range of specified operating conditions. However, the process by which ions are extracted from the discharge plasma, prior to their acceleration and focusing by the accelerator system, is not well understood. It is known that a plasma sheath is formed and that this sheath is a transition region separating the discharge plasma (i.e., the ion production region where local ion and electron number densities are equal) from the ion acceleration region where ions only are present. This

plasma sheath is expected to vary in position and shape as a result of plasma density (i.e., beam current), accelerator system geometry and accelerator system potential variations. Knowledge of how these parameters affect the physical characteristics of the plasma sheath would advance the understanding of the role this sheath plays in ion optical phenomena. These physical characteristics include, the divergence of the beam ions ejected from the accelerator system, the efficiency with which ions are extracted from the discharge plasma, the ion bombardment and erosion of various accelerator system components and the limit to the ion current which can be extracted from the plasma.

Some theoretical and experimental work has been done to determine the physical characteristics of the plasma sheath transition region separating the discharge plasma and ion accelerator system.[2,4,5,8-10] However, the theoretical model predictions are somewhat conjectural since they rely on various initial assumptions which may not necessarily be valid in the actual physical situation. This suspicion is reinforced with earlier work by the author[3,6,7] showing serious discrepancies between theoretically predicted and experimentally observed ion beam divergence characteristics of various ion accelerator systems. These discrepancies are believed to result from the inability of the theoretical models to describe the plasma sheath transition region adequately. Similarly, the available experimental data is limited to a couple of idealized cases; which are photographic in nature and present the plasma sheath as a discontinuity and are of limited use. Therefore, a thorough experimental investigation of the physical structure and behavior of the plasma sheath adjacent to an ion accelerator system was undertaken. The basic physical phenomena uncovered

would provide a substantially better understanding of the ion extraction and pre-ion acceleration process from a plasma and aid in the development of improved theoretical models.

ACCELERATOR SYSTEM SCALING

Ion Beam Formation

Most ion accelerator systems consist of either two or three grids
(i.e., electrodes) with each grid perforated by numerous holes, usually
in a hexagonal array. These grids are electrically isolated from each
other and orientated so that their holes are aligned. The assembled
accelerator system is positioned adjacent to a discharge chamber capable
of producing the desired plasma conditions. Ion* acceleration is
achieved by applying a potential distribution to the accelerator system
such that plasma electrons are repulsed and plasma ions are accelerated
by the applied electrostatic body forces. Figure 1a depicts a portion
of a multi-aperture two-grid ion accelerator system showing the coaxial
hole geometry and ion beamlet formation. Figure 1b illustrates the
variation in electrical potential associated with the grid geometry of
Fig. 1a. As shown in Fig. 1b, the discharge chamber is at a potential
a few tens of volts positive of the screen grid which is at a high
positive potential. The purpose of the screen grid is to prevent di-
rect access of the accelerated ions to the accelerator grid webbing.
It is the accelerator grid, with its high negative potential, that
actually accelerates the ions from the discharge plasma. A third,
decelerator grid, may be positioned after the accelerator grid. This
grid is usually maintained at facility ground potential and can reduce
ion beam divergence significantly.[4,7]

---

*Here, as in the following sections, positive ions only are being
considered.

a)

b)
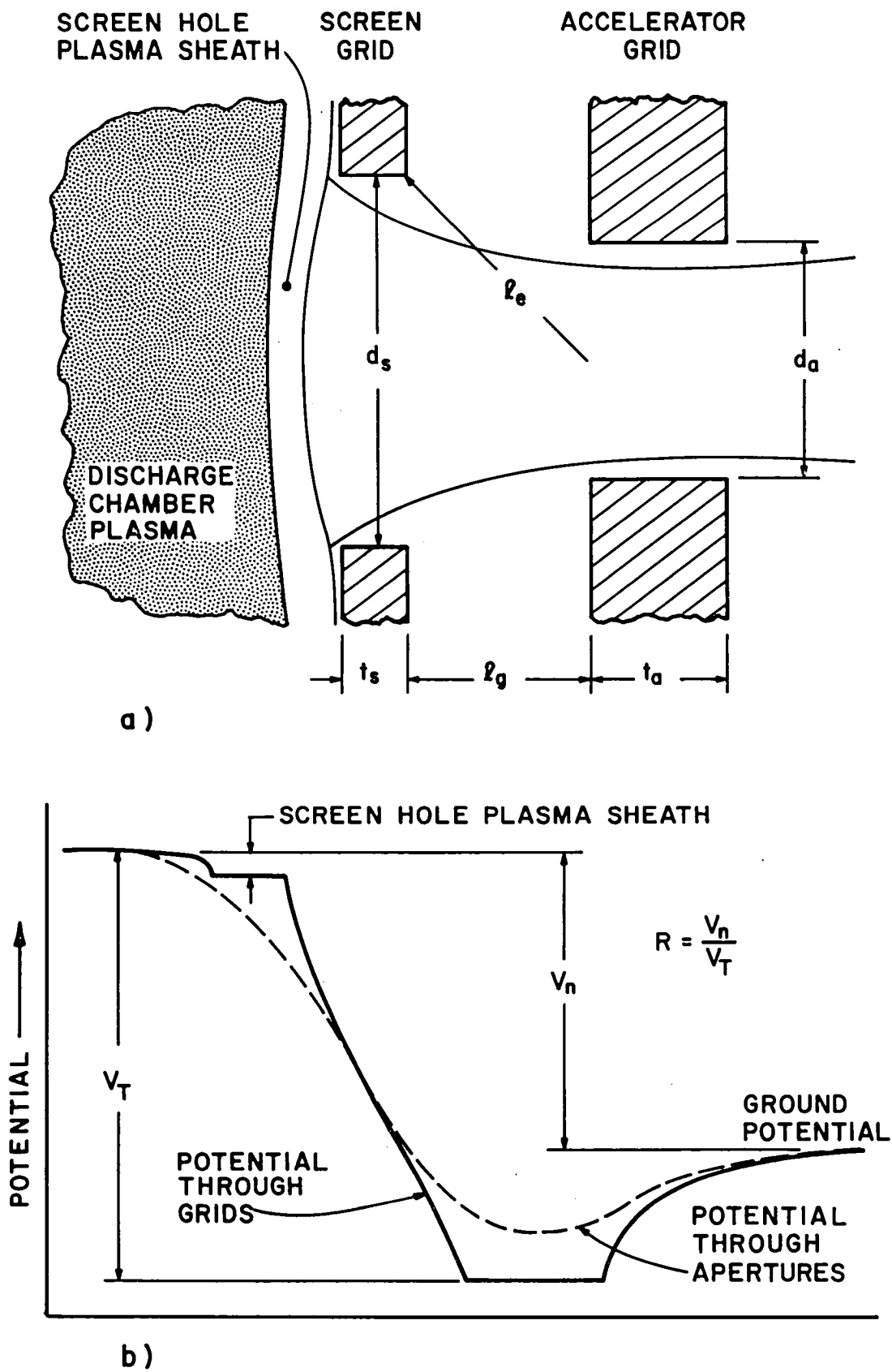
Fig. 1 a) Accelerator system geometry.
b) Accelerator system potential variation.

The simple two-grid ion accelerator system shown in Fig. 1 embodies those principles of operation of most importance to the physical phenomena occurring in the screen hole plasma sheath transition region. It is in this region that the plasma electrons begin to feel the effect of the negative accelerator grid and are retarded. Since the plasma electrons have a distribution of energies, their penetration depth into the ion accelerator system is varied; giving rise to the large extent of screen hole plasma sheath depicted in Fig. 1a.

Geometric Similarity

In order to make accurate measurements of the physical characteristics of the screen hole plasma sheath (i.e., position, shape and structure), it was necessary to use a large accelerator system so adequate spatial resolution could be achieved. This was done by increasing the screen hole diameter from a value of 2.0 mm, which is typical of ion thruster and ground application ion source accelerator system designs and where the screen hole plasma sheath width was estimated to be $\sim$ 0.3 mm, to a diameter of 12.7 mm where a plasma sheath width of $\sim$ 2.0 mm was estimated. The other geometrical accelerator system parameters were also scaled directly by the ratio of these two diameters so geometric similarity was maintained. It was important to determine whether the maximum normalized perveance per hole[6] and ion beam divergence characteristics of such large accelerator systems were any different from the much smaller accelerator systems typical of most ion sources. Careful probing of the ion beam emerging from the large accelerator systems showed the divergence characteristics of these grid sets were identical, within experimental error ($\sim$ $\pm$1.0°), to those of the smaller accelerator systems. Typical results are presented in

Table 1 where the ion beam divergence angle has been defined as the cone half angle, α, enclosing 95% of the total beam current.[6]

TABLE 1. Large Accelerator System Ion
Beam Divergence Characteristics.

NP/H $(amp/volt^{3/2})$	α, measured (degrees)	α, predicted[6] (degrees)
1.08×10^{-9}	16.0	15.9
2.17×10^{-9}	11.3	12.4
3.25×10^{-9}	11.5	12.5

Figure 2 shows the effect of screen hole diameter variations on the maximum normalized perveance per hole for grid sets having similar nondimensionalized geometric parameters. Here, the total accelerating voltage V_T, the discharge voltage V_D and the net-to-total accelerating voltage ratio R were held constant at the values indicated. These parameters were not dependent on the accelerator system geometry scale changes. From Fig. 2 it is evident that there is little effect on the maximum normalized perveance per hole as the screen hole diameter is increased above 2.0 mm. The significance of this result can be fully appreciated when it is understood that a screen hole diameter change of 2.0 to 12.7 mm corresponded to a factor of fourty decrease in beam current density. It is not important here, but some effects have been found for smaller screen hole diameters than 2.0 mm.[6]

In summary, scaling up ion accelerator systems to larger sizes does not appear to affect ion beam divergence characteristics or the
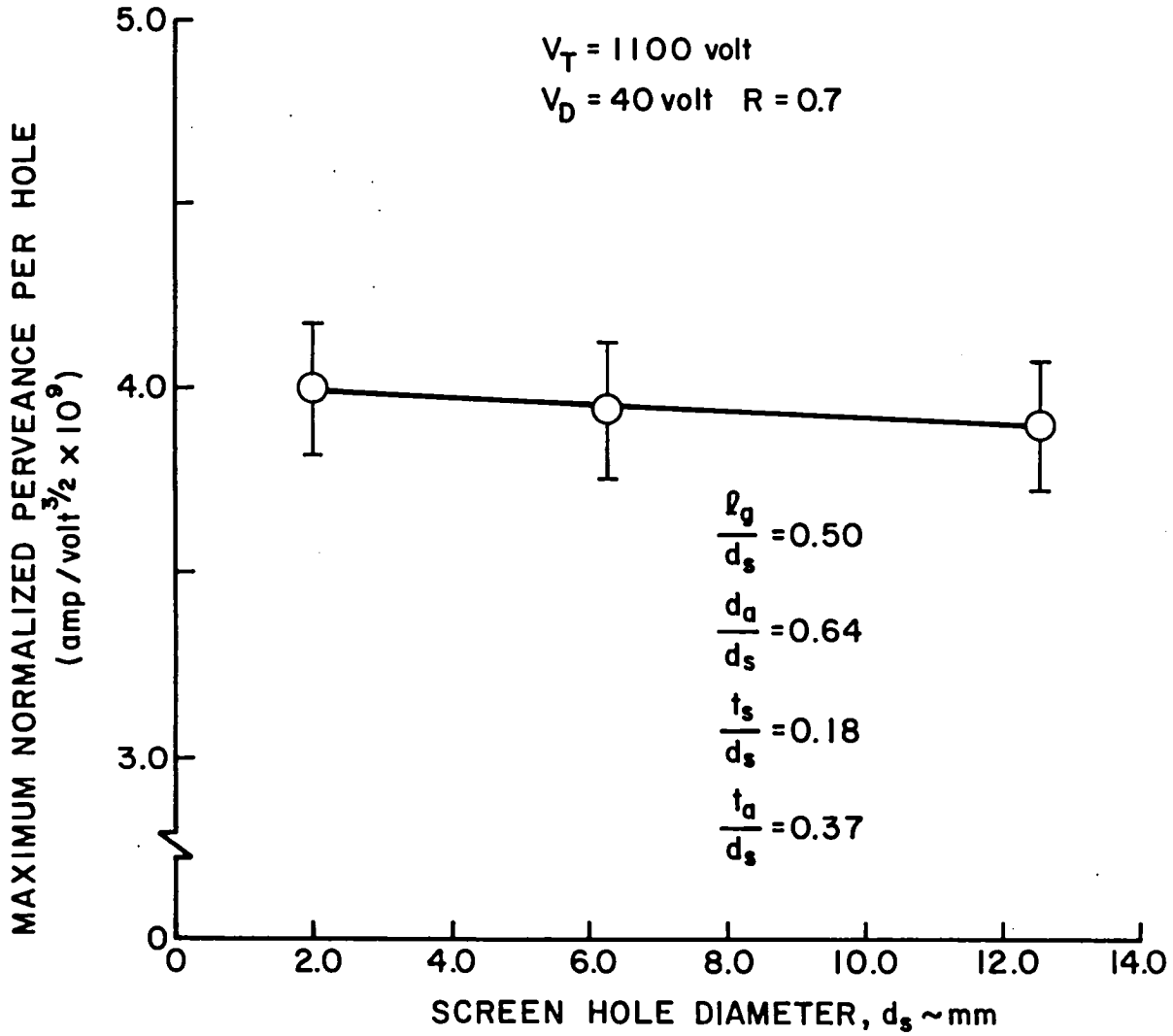
Fig. 2 Effect of screen hole diameter variations on the
maximum normalized perveance per hole.

maximum normalized perveance per hole as long as similar nondimensionalized grid parameters are maintained. This result indicates that the screen hole plasma sheath characteristics would also scale with accelerator system scale changes.

APPARATUS AND PROCEDURE

Sheath Probing Technique

The screen hole plasma sheath was investigated at various grid geometry and accelerator system operating conditions. Figure 3 indicates the manner in which these data were obtained. In Fig. 3a a cross sectional view of the large seven hole two-grid accelerator system used for this study is depicted. Both the screen and accelerator grids were made from high purity sheet graphite. This material may be machined easily and is stable dimensionally at the high operating temperatures typical of this experiment ($\sim$ 420°C). A seven hole hexagonal geometry was used for the accelerator system. With this aperture arrangement the central screen hole was surrounded by adjacent screen hole sheaths. In this manner, the central screen hole modelled a screen hole typical of a conventional ion accelerator system employing many thousands of apertures. The probing volume surrounding the central screen hole is shown by the dotted rectangle in Fig. 3a. The probe origin was set at the downstream face of the screen grid and the sheath was probed a distance of one screen hole diameter back into the discharge plasma from this point. The width of the probing region was 1.4 d_s (d_s = screen hole diameter) in order that sufficient data points could be taken to define the sheath overlap region adjacent to the screen grid webbing.

Figure 3b indicates the manner in which the probe traversed the central screen hole. The sheath probe was set at each of the fifteen equidistant radial locations shown. At each location, the probe was swept axially through the sheath and the variation in local plasma

a)

b)
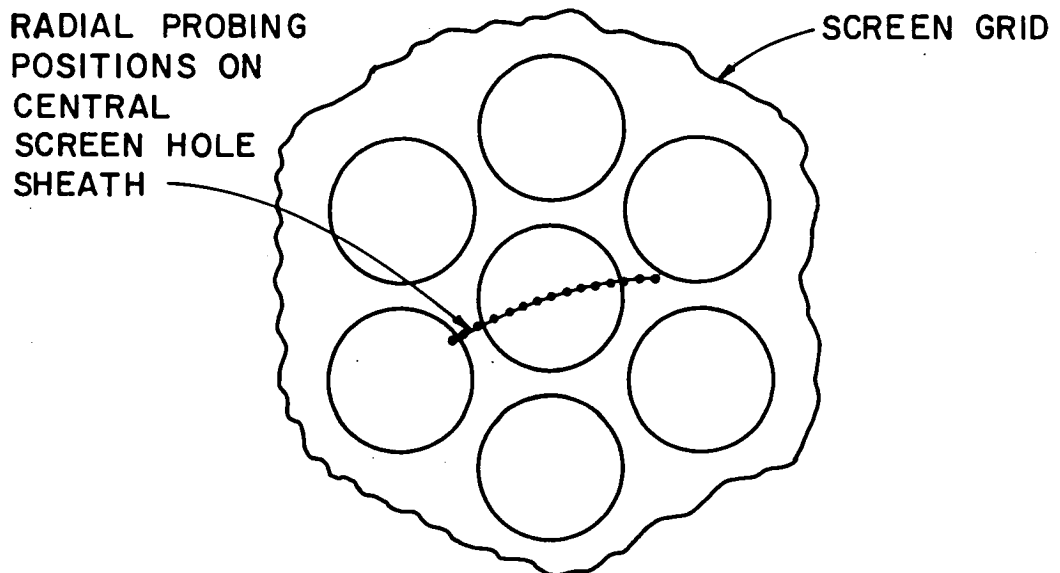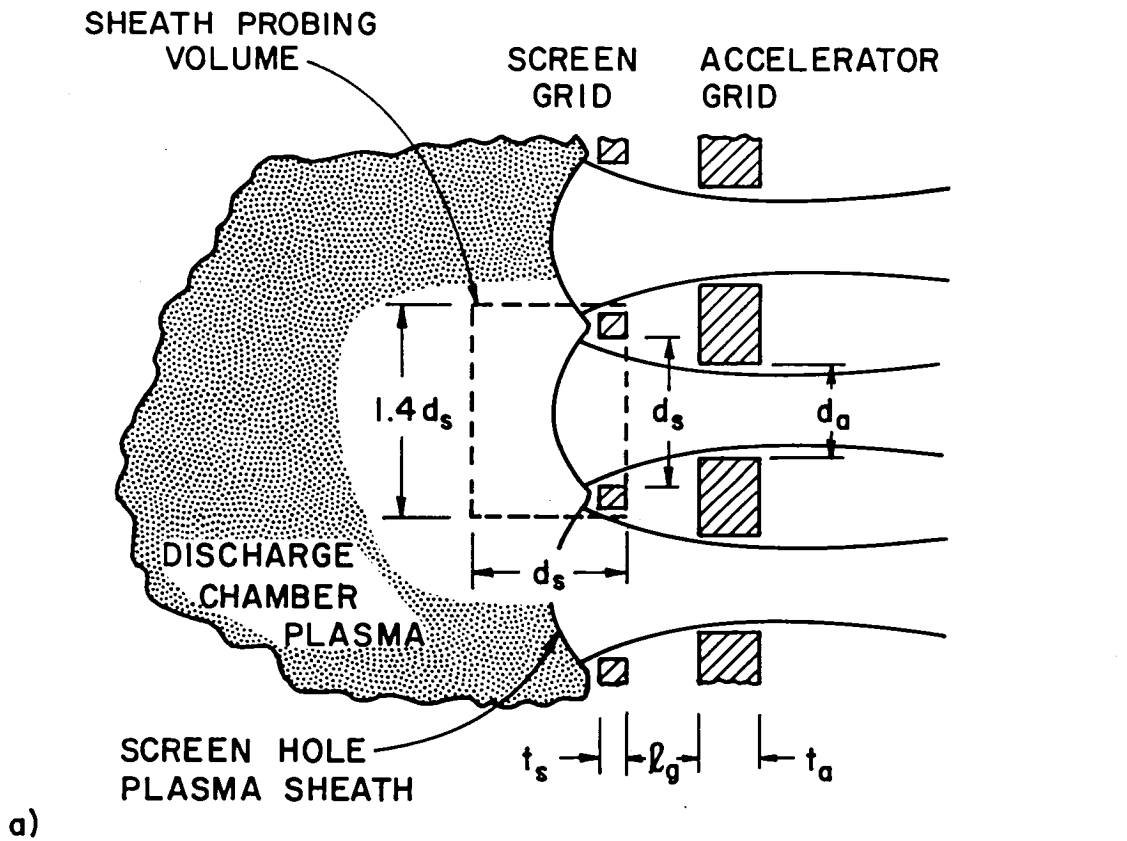
Fig. 3 a) Screen hole sheath probing volume.

b) Sheath probe location.

potential was recorded. In this way a full sheath profile, for a particular accelerator system geometry and operating condition, was characterized by an array of local plasma potential values.

Ion Source Design

The accelerator system depicted in Fig. 3 was positioned over the masked down discharge chamber of an 8 cm diameter electron-bombardment ion source. This ion source had a mildly divergent magnetic field and used tungsten wire filaments as both the main and neutralizer cathode emitters. Argon propellant was used and all source operation was conducted in a 30-cm dia. pyrex bell jar. Average bell jar pressure was 2.3×10^{-4} torr.

Ion source plasma conditions were determined from a small spherical Langmuir probe located inside the discharge chamber. This probe was offset slightly from the ion source axis and could be moved axially over a distance of some 3.0 cm within the discharge chamber. Plasma property measurements obtained with this probe were plasma potential V_p, electron density n_e and ion density n_i, Maxwellian electron temperature T_m and the primary-to-Maxwellian electron number density ratio n_p/n_m. Appendix A details the manner in which the spherical Langmuir probe traces were analysed to yield these parameters.

Sheath Probe Design

A floating emissive Langmuir probe[11] was used to study the screen hole plasma sheath and is shown in Fig. 4a. This probe had a simple dog leg shape so it could be positioned off the axis of the central screen hole thereby permitting the probe tip to move radially as the probe was rotated (Fig. 3b). An enlarged drawing of the probe tip is

TWIN BORE ALUMINA
TUBING 1.57mm O.D.
×0.40mm BORE DIA.

0.076mm DIA.
TUNGSTEN/26%
RHENIUM FILAMENT
WIRE

2.0mm

0.3 mm

ALUMINA TUBING
2.36mm O.D. ×
1.60mm I.D.
ENCLOSING
REFRACTORY
CO-AXIAL WIRE

0.3 mm DIA.
NICKEL WIRES
SPOT WELDED
TO FILAMENT

SAUEREISAN
ELECTRIC
RESISTOR
CEMENT

TO PROBE
MEASURING CIRCUIT

a)

EMISSIVE PROBE
FILAMENT

HIGH IMPEDANCE
ELECTROMETER

BATTERY FILAMENT
HEATER SUPPLY

V

TO SCREEN
POTENTIAL

b)

Fig. 4 a) Sheath probe design details.

b) Circuit schematic for floating potential
measurements.

shown also to detail the basic construction of the probe filament, its
pertinent dimensions and its attachment to the nickel support wires.
In operation, the sheath probe is electrically isolated from the dis-
charge chamber body and when the filament is heated to incandescence
the filament floats at a potential very near the local plasma potential.
This unique behavior of a floating emissive probe occurs for the
following reason. Since the probe is floating, the net current at the
filament surface must be zero. If the filament is cold (i.e., not
electron emitting) this means an equal flux of plasma ions and elec-
trons must arrive at the filament surface. However, because ions are
so much heavier than electrons and their energy (for the electron bom-
bardment discharge plasma under consideration) is less, they move con-
siderable slower. Consequently, the initial electron flux to the
floating filament surface greatly exceeds the ion flux. These electrons
rapidly impress a negative potential upon the filament, impeding further
electron flow until the equilibrium situation of equal ion and electron
arrival rates is reached. The electron space charge so developed would
ordinarily force the floating filament to assume a potential consider-
ably negative of the surrounding plasma. The magnitude of this negative
potential being of the order of the most energetic plasma electrons
(tens of volts). If however, the filament is then heated to electron
emitting temperatures the filament electrons so produced are accelerated
away from the filament surface into the more positive plasma surround-
ing it. In so doing, the filament electrons can neutralize the plasma
electron space charge. This space charge neutralization is aided by
increased filament electron emission with filament temperature increases.
An equilbrium situation is quickly reached with the filament floating

very near plasma potential. Under these conditions, the flux of plasma electrons to the filament is countered by the outflux of filament electrons, which while possessing significantly lower energies can be produced in much greater numbers (at least for the plasma densities under consideration in this experiment $\sim 10^{15}$ m^{-3}). Provided a sufficient filament electron temperature is maintained, to ensure adequate electron emission, the emissive probe floating potential will follow closely local plasma potential changes.

The instrumentation used to measure the probe floating potential is shown schematically in Fig. 4b. Briefly, an isolated battery supply provided heating power to the filament. The filament was connected through this battery supply to a high impedance electrometer set to measure voltage; the low side of the electrometer was referenced to screen grid potential. An emissive Langmuir probe characteristic showing the probe floating potential variation observed on the electrometer as a function of filament heater current is shown in Fig. 5. From Fig. 5 it can be seen that with the filament heater current between 1.1 and 1.3 amperes the observed probe floating potential is not very different from the actual plasma potential. Indeed, rather than take individual probe traces, the probe filament heater current was maintained constant at 1.2 ampere and the local plasma potential variation recorded directly as the probe was moved through the screen hole plasma sheath.

Sheath Probe Error

Floating emissive Langmuir probes of the design shown in Fig. 4 have an inherent error originating from the small D.C. voltage
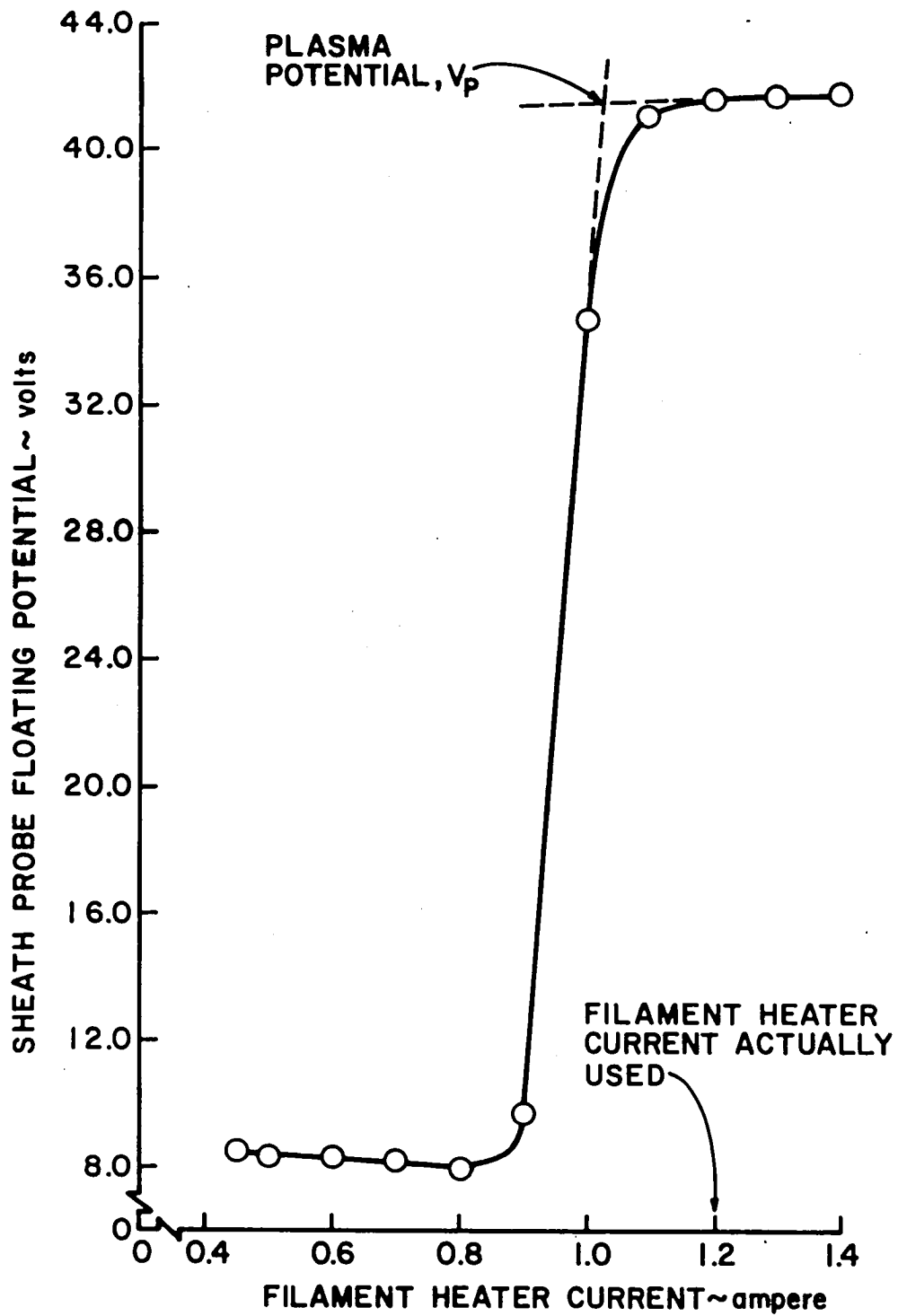
Fig. 5 Effect of filament heater current on the emissive sheath probe floating potential.

extending along the length of the heated filament. This potential drop was approximately 0.5 volt in this experiment. Another, more serious source of possible error when using constant battery supplied heating current, is the requirement of zero potential difference between the filament tip and electrometer input terminal. Figure 6 illustrates the circuit used to null this spurious voltage in this experiment. Briefly, the probe filament was heated by a 1.2 ampere current. The heated probe was then brought into contact with the discharge plasma (or upstream) side of the screen grid so that the incandescent filament was barely touching its surface. The nulling potentiometer depicted in Fig. 6 was then adjusted until the parallel resistance probe heating circuit was balanced and zero potential was observed between the filament tip and electrometer input. The sudden decrease in the electrometer potential reading when the heated filament tip touched the screen grid was also the manner by which a reference probe axial position was obtained. Both the nulling and probe position referencing technique were extremely reliable and did not require continual adjustment.

Another, more subtle, source of sheath probe error is associated with the magnitude of the double sheath which must surround a floating emissive probe. This double sheath forces an emissive probe to float somewhat negative of the surrounding plasma and is a consequence of the filament electron energy being considerably smaller than the plasma electron energy. Appendix B contains a theoretical derivation of the magnitude of this error, which suggests that a maximum error of one volt was to be expected.

In practice, the screen hole sheath probe accuracy was checked by comparing plasma potential measurements obtained with it and with the

SHEATH PROBE
FILAMENT

HIGH IMPEDANCE
TO GROUND VACUUM
FEEDTHROUGH

0-2 amp. (A)

0-10,000 ohm
NULLING POT.

6800 ohm

TO ELECTROMETER
INPUT

0-25 ohm

0-25 ohm

TWO 12 volt, 5 ah
LEAD/ACID BATT.

TO SCREEN GRID
POTENTIAL
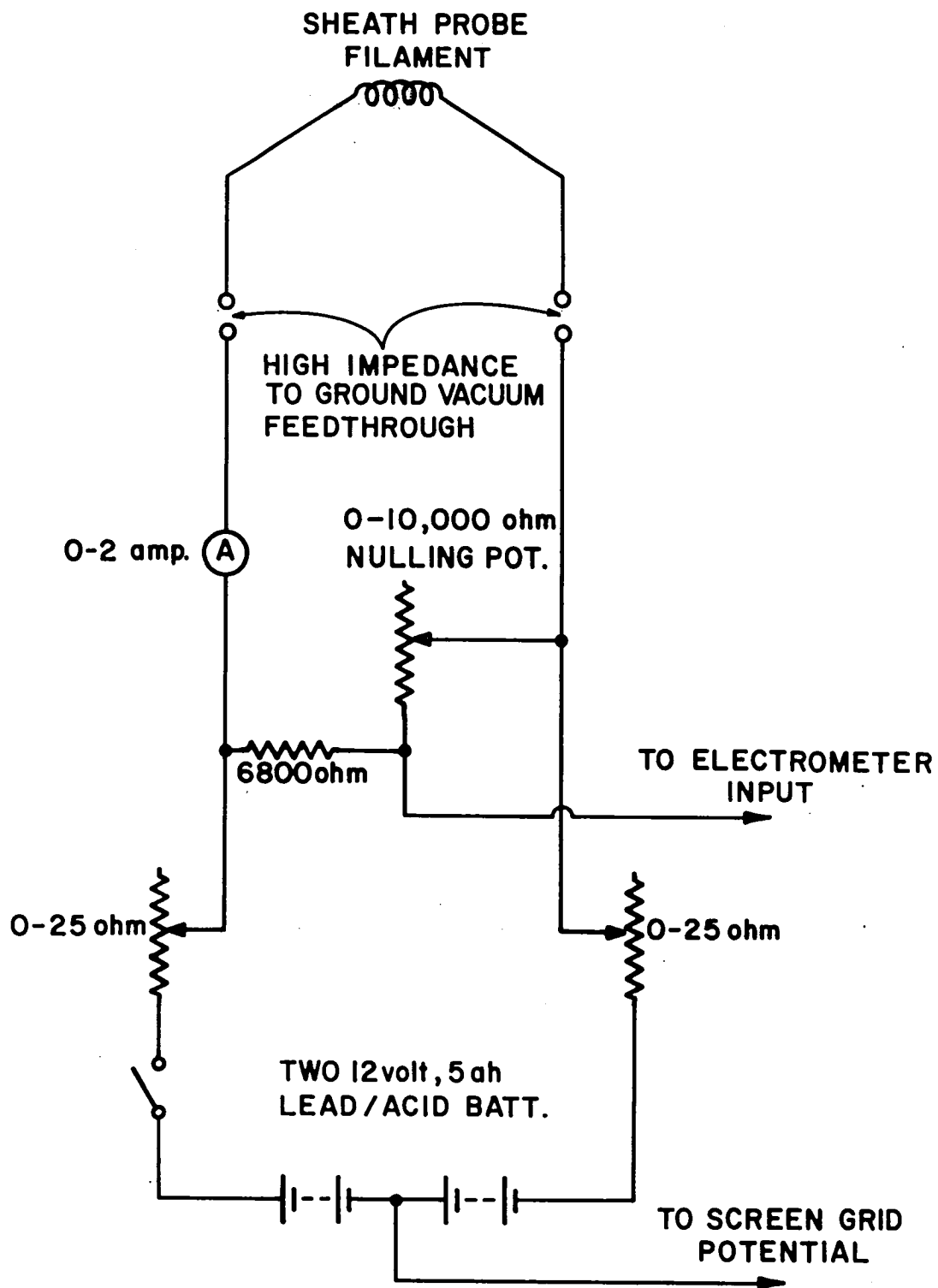
Fig. 6 Sheath probe voltage nulling circuit.

small spherical probe described earlier. The screen hole sheath probe consistantly gave lower readings but the difference was less than 5% of the spherical probe plasma potential readings in all cases. A more detailed discussion of the operating characteristics of floating emissive Langmuir probes is presented by Kemp and Sellen.[12] The positioning error of the sheath probe was $\pm$ 0.004 d_s in the axial direction and $\pm$ 0.02 d_s in the radial direction.

Sheath Contour Data Reduction

The screen hole plasma sheath is really the set of equipotential lines that separate the region of homogeneous discharge plasma from the region of accelerated ions where there are no electrons. Equipotential contours describing this intermediate region were computer drawn from the array of data obtained after probing each screen hole sheath profile for each operating condition. First, each set of twenty axial sheath potential values, obtained directly from the sheath probe at each of the radial probing locations shown in Fig. 3b, was handled by a cubic spline interpolation routine. This computer routine produced fifty-one interpolated sheath potential values. Each of these points was separated by a distance of 0.02 d_s and together extended a distance of one screen hole diameter (1.0 d_s) into the discharge chamber from the downstream screen grid origin. These fifty-one sheath potential values were curve fitted using a 10th order orthogonal polynomial regression analysis. Sheath potential values determined using the polynomial expression obtained from this regression analysis were then free of most of the scatter contained in the original data points. This scatter reduction was very important for electron and ion number density

calculations through the sheath. These calculations will be discussed in more detail later.

Figure 7 is a plot of the twenty actual data points and the fifty-one points determined from the regression analysis polynomial for the sheath potential variation along the center line of a typical grid set for a standard operating condition. The agreement is excellent. The data in Fig. 7 has been normalized to a sheath potential one screen hole diameter back from the downstream screen grid face (the probing origin). The subsequent sheath potentials are negative to reflect the fact that the potential in the screen hole plasma sheath is less than that of the discharge plasma. Although interpolation routines were used for the axial sheath potential distribution, no such interpolation was done for the radial sheath potential variation when the sheath potential contours were plotted.
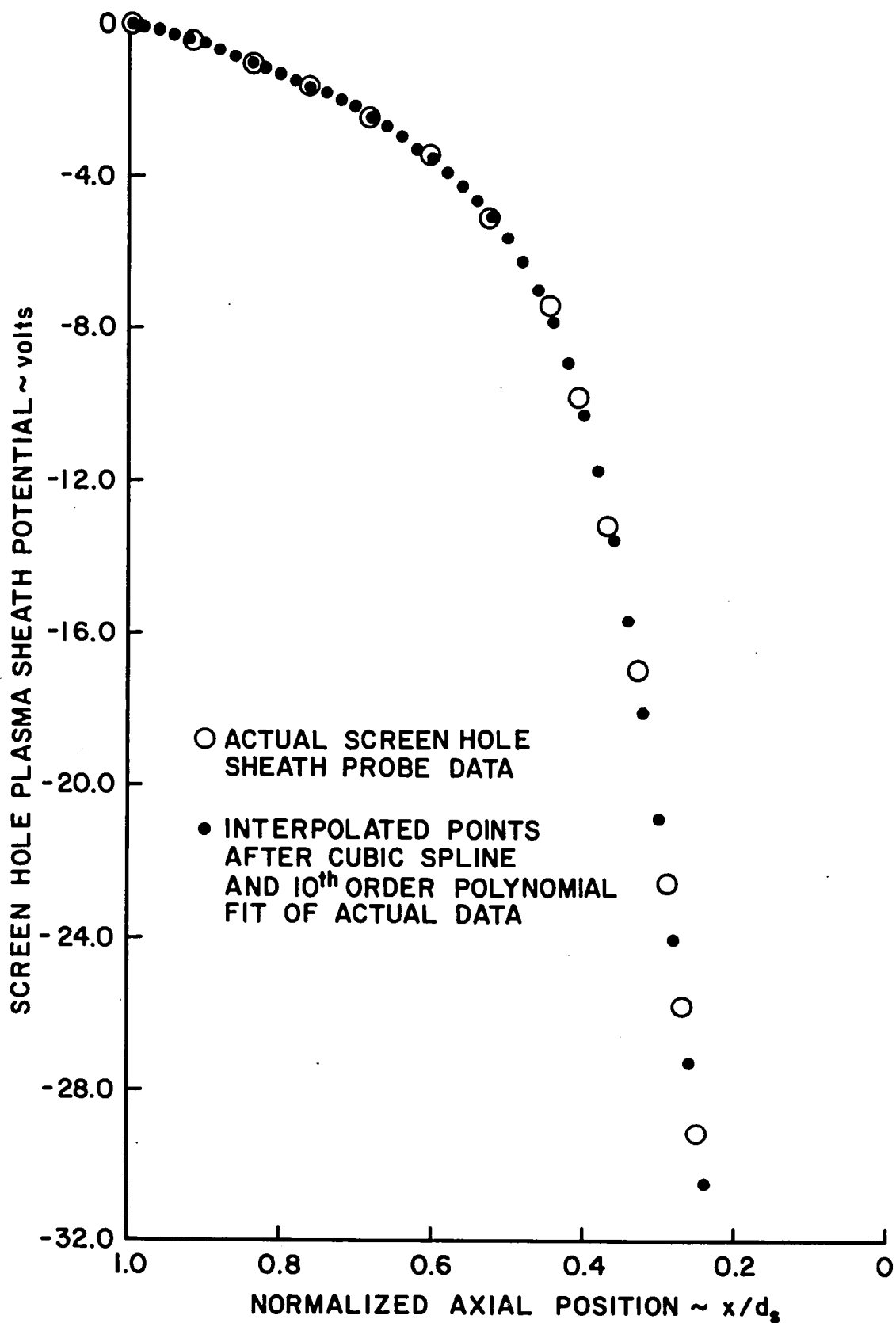
Fig. 7 Comparison of experimentally obtained and interpolated sheath potential values.

RESULTS AND DISCUSSION

Unless indicated otherwise, the following grid geometry and accelerator system operating conditions may be assumed:

center-to-center hole spacing,		= 14.7 mm
screen hole diameter,	d_s	= 12.7 mm
total accelerating voltage,	V_T	= 1100 volts
net-to-total accelerating voltage ratio,	R	= 0.7
screen grid thickness ratio,	t_s/d_s	= 0.18
accelerator hole diameter ratio,	d_a/d_s	= 0.64
accelerator grid thickness ratio,	t_a/d_s	= 0.37 .

Effect of Plasma Density Variations

Figure 8 shows the screen hole plasma sheath, represented as a set of equipotential contours, for the central screen hole of the large seven hole two-grid set shown in Fig. 3. The central screen hole in Fig. 8 is a cross sectional view and is drawn to scale as are the equipotential contours. It should be noted that the path traced out by the sheath probe in Fig. 3b crosses the webbing of the adjacent screen holes at different locations. These locations were not always the same as those shown in Fig. 3b because each grid geometry tested was not orientated in exactly the same way about the center line of the ion source discharge chamber. Consequently, the path traced out by the probe, although always passing through the screen hole axis and being set at the same radial positions, did vary somewhat relative to the adjacent screen holes. To indicate this possible variation, the cross sectional view of the screen hole in Fig. 8 has the screen grid webbing

$NP/H = 2.50 \times 10^{-9}$ amp/volt$^{3/2}$
$\ell_g/d_s = 0.50$
$V_D = 45.0$ volts
CONTOUR FROM 0.0 TO -25.0 volts
CONTOUR INTERVAL OF 1.0 volt
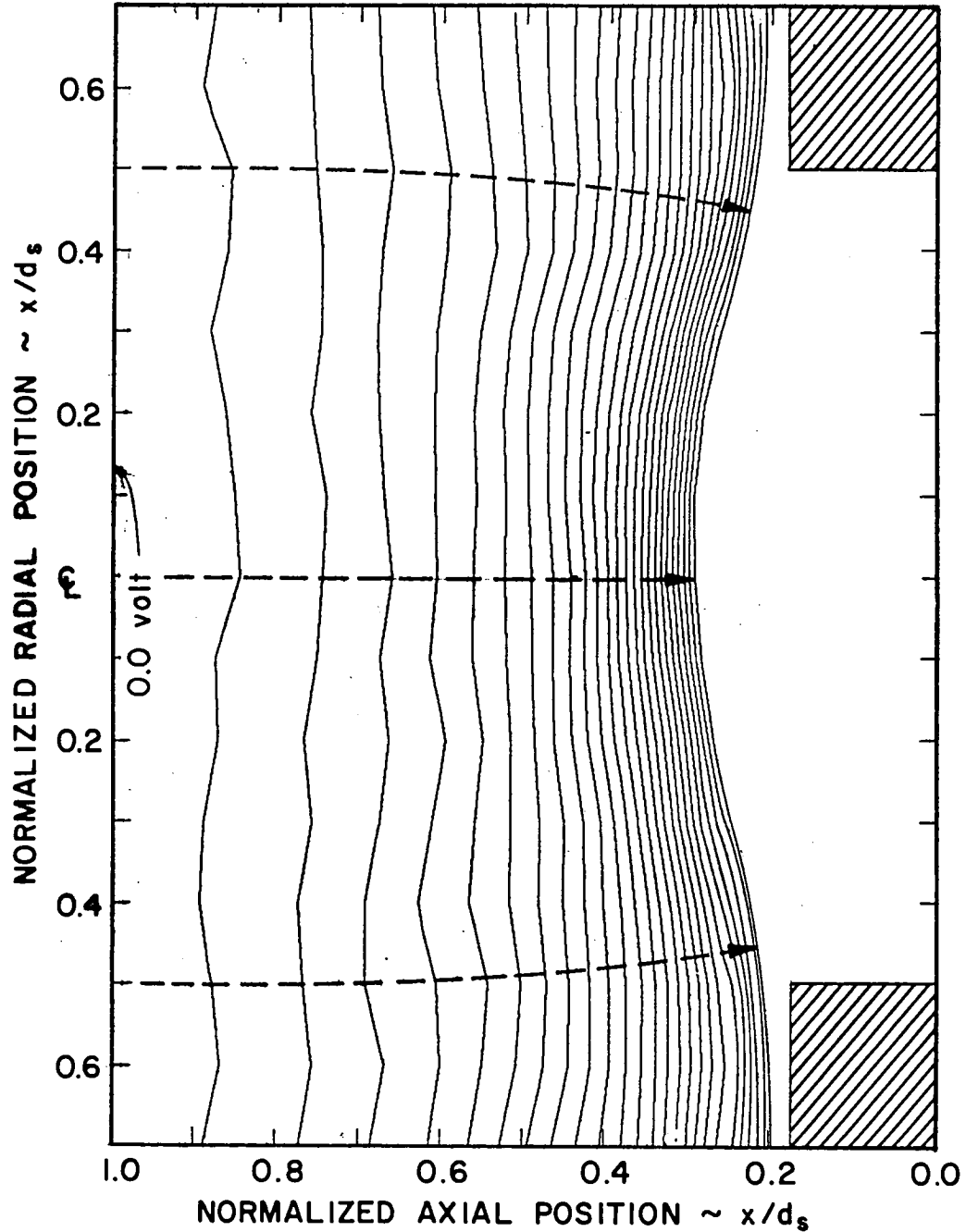
Fig. 8 Full screen hole sheath profile for standard

grid set geometry and operating conditions.

extended out to the extremities of the probing volume, without regard to the actual location of the adjacent hole.

The grid set used in Fig. 8 had an intermediate screen-to-accelerator grid separation ratio, ℓ_g/d_s, of 0.50 and a discharge voltage, V_D, of 45.0 volts. This grid set was operated at a beam current or normalized perveance per hole value known to give the lowest ion beam divergence.[6] As mentioned previously, the sheath potential at a distance of one screen hole diameter back from the probing origin was defined as zero volts. Equipotential contours were plotted at one volt increments relative to this zero reference potential and are shown extending to -25.0 volts (the plasma sheath potential being below that of the discharge, or bulk, plasma). The -25.0 volt contour line is very close to what was considered the sheath boundary. At this location the local electron density was only about 10% of the bulk plasma electron density. If the probe was moved much beyond this point no plasma electrons were detected and the probe accumulated a positive charge because of the incident ion flux.

The sheath surrounding the central screen hole of Fig. 8 is fairly symmetrical; the very slight asymmetry is believed to be due to the sheath probe entering different regions of the screen grid webbing at the extremities of its travel (Fig. 3b). The uncertainty in the axial location of the sheath potential contours was related directly to the spatial resolution which was $\sim 0.02 \, d_s$ throughout these tests. Electric field vectors plotted normal to the equipotential contours give a fair estimation of actual ion trajectories (Appendix C). These vectors show how the average ion motion is directed through the screen hole as a consequence of the ion accelerating fields of the negative accelerator grid.

Perhaps the most important conclusion to draw from Fig. 8 is that the screen hole plasma sheath extends over a large distance, influencing ion and electron trajectories deep within the discharge chamber plasma. To illustrate this point, the Debye length for the plasma condition shown in Fig. 8 was 0.05 d_s, whereas significant potential variations are evident over distances at least fifteen times this value. This result supports theoretical sheath width predictions of Grisham et. al.[5] who have calculated potential distributions and ion trajectories for various ion accelerator systems. The work of Grisham et. al. and theoretical models developed by other authors will be discussed in greater detail in later sections of this report.

Figure 9 makes a comparison between the sheath surrounding the central screen hole of the large seven hole two-grid set and the sheath surrounding one of the edge holes of this grid set. For clarity, only the -5.0, -15.0 and -25.0 volt contours are plotted in each case. Again, an intermediate grid separation was used and the grid set was operated at a normalized perveance per hole known to give the minimum beam divergence. Sheath distortion is evident for the edge hole. This distortion tends to direct the initial ion trajectories to greater off axis angles, as evidenced by the electric field lines drawn in Fig. 9. Plasma density variations across the edge hole were primarily responsible for the sheath distortion shown in Fig. 9. An edge hole was probed also in a situation where the plasma density was known to be uniform. Under these circumstances, much less significant screen hole sheath distortion was evident. It has been well documented[18] that those ions emerging from the outer holes in a multiaperture accelerator system have very divergent trajectories and cause serious accelerator grid sputter

$NP/H = 2.50 \times 10^{-9}\, amp/volt^{3/2}$

$\ell_g/d_s = 0.50$

$V_D = 45.0\, volts$

CONTOUR FROM -5.0 TO $-25.0\, volts$

CONTOUR INTERVAL OF $10.0\, volts$
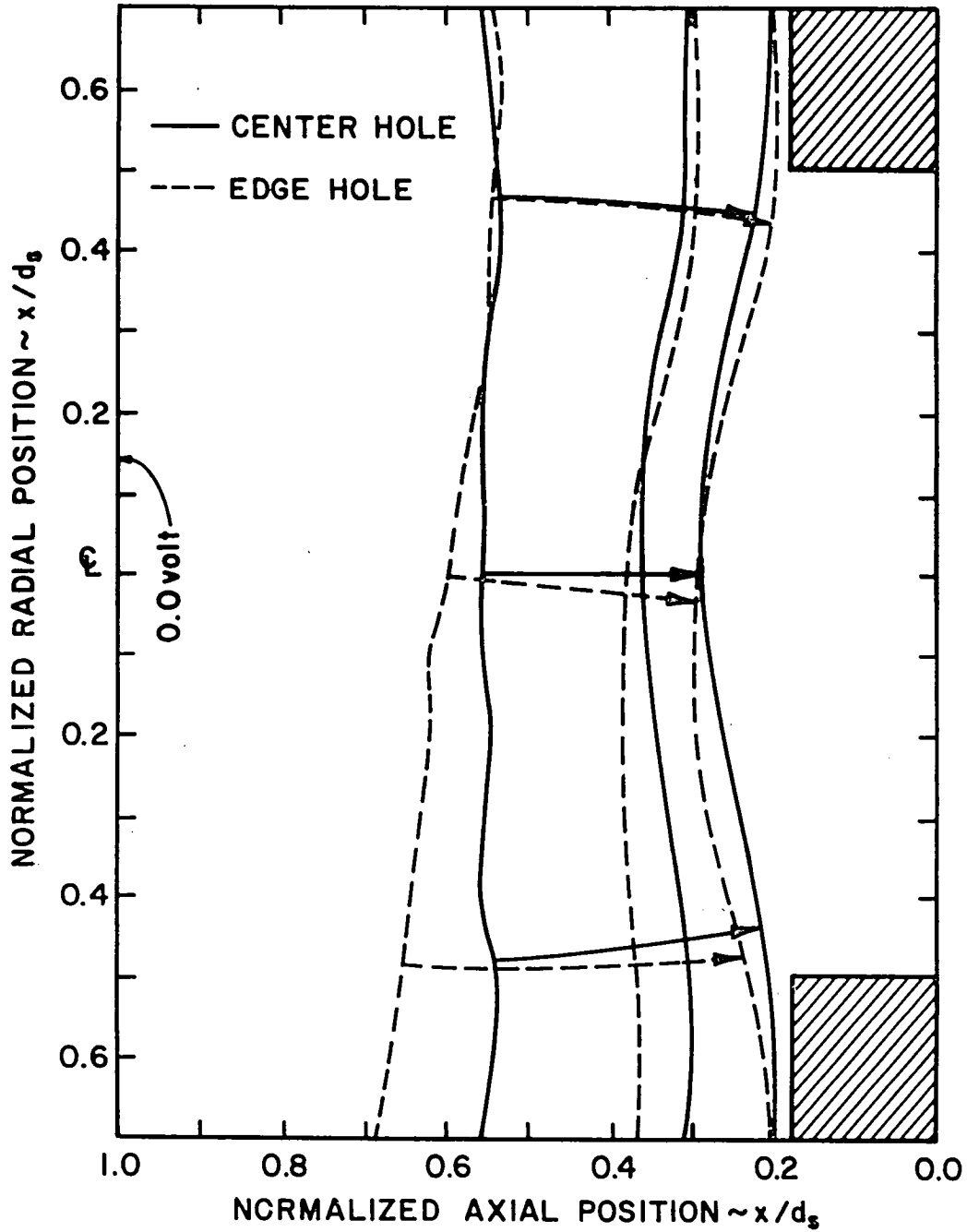
Fig. 9 Comparison of center and edge hole sheath potential
contours (grid set edge towards vottom of figure).

erosion. The results of this study indicate that the decrease in plasma density as the discharge chamber edge is approached distorts the edge screen hole plasma sheaths giving rise to more divergent ion trajectories. The lack of adjacent screen hole sheath interactions for an edge hole does not significantly contribute to this sheath distortion and ion defocusing effect. These results support earlier observations by Kaufman.[4]

Effect of Beam Current

Previous experimental results [1,3,6,7] have shown that for a given total accelerating voltage ion beam focusing is poor at very low and very high beam currents. The best ion beam focusing occurs at a beam current intermediate of these two extremes. To investigate the mechanism of this focusing effect, the screen hole plasma sheath was probed during grid set operation at very low and very high normalized perveance per hole values. The screen hole sheath profiles determined from this probing are shown in Fig. 10 for the same grid set geometry as that used in Fig. 8. Here, the central screen hole of the large seven hole accelerator system described previously was probed. Since the central screen hole sheath is fairly symmetrical (Fig. 8), only a half sheath profile is being presented.

Figure 10 shows that at low normalized perveance per hole (or beam current) values the sheath boundary (i.e., the -25.0 volt contour line) is quite bowed and extends a considerable distance into the discharge chamber. By examining the electric field vectors, or ion trajectories, at the periphery of the sheath boundary, it is apparent that the ions emerging from this region have significant velocity components perpendicular to the screen hole axis. It is believed that these large
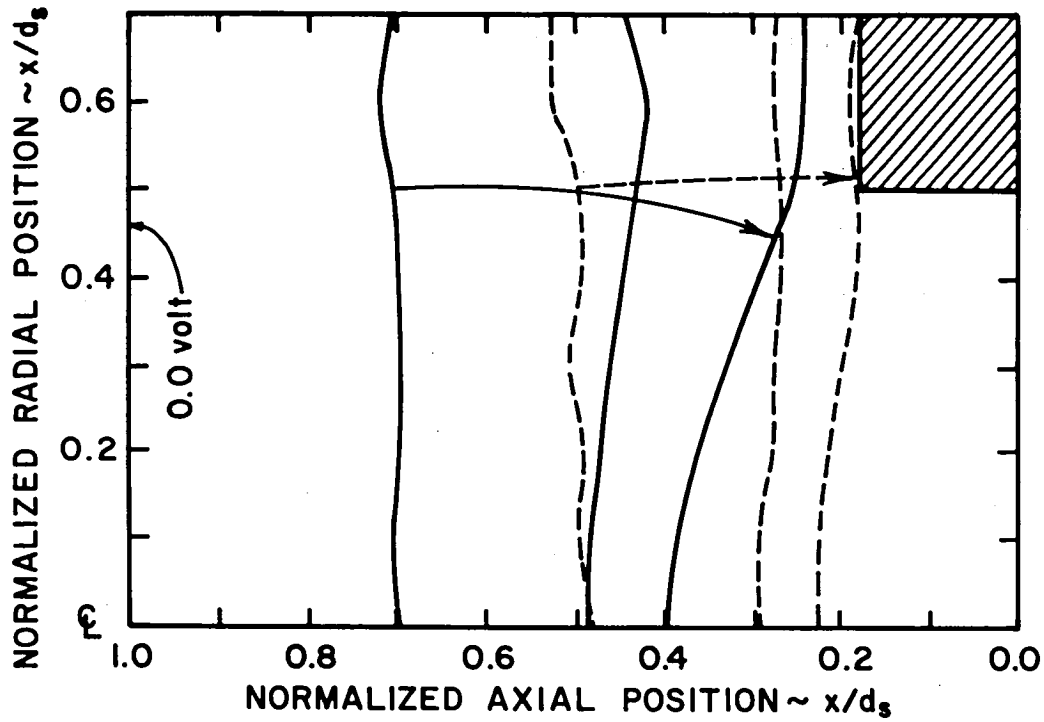
Fig. 10 Screen hole sheath movement and shape change with increasing beam current, or normalized perveance per hole, (half sheath profile).

off-axis ion velocity components produce the very divergent ion beam that is associated with grid set operation at low ion beam currents. Conversely, increasing the normalized perveance per hole, or beam current, by increasing the discharge chamber plasma density through increased cathode electron emission, moved the sheath closer to the screen hole and the sheath boundary became almost planar in shape. The trajectories of those ions emerging from the peripheral region of the sheath boundary (dashed arrow in Fig. 10) are now, if anything, directed slightly away from the screen hole axis; resulting in an ion beamlet that is fanning out at its extremities. It is believed that at this high beam current condition, such a large number of ions are being drawn through the accelerator system that electrostatic repulsion forces are fanning out the peripheral beamlet ions giving rise to poor ion beam focusing.

The results of Fig. 10 indicate that the good focusing characteristics of beam currents intermediate of the two extremes shown are a result of a sheath boundary shape which gives minimum off-axis ion velocity components at an ion current density low enough to give negligible electrostatic repulsion effects. Figure 10 also shows that for the large normalized perveance per hole condition (dashed contour lines) the screen hole plasma sheath did not enter the screen hole. Previously, it had always been assumed that an ion accelerator system operating near its maximum normalized perveance per hole condition (as was the case for the dashed contour lines in Fig. 10) must have the screen hole plasma sheath located within the screen hole. A detailed experimental investigation accounting for this behavior is presented in a later section.

Effect of Grid Separation

Figure 11 compares the effect on the screen hole plasma sheath as the separation distance between the screen and accelerator grids was varied. In all cases the grid sets were operated at a normalized perveance per hole value known to give the lowest ion beam divergence for that particular grid separation.[6] For clarity, only the -10.0 and -20.0 volt contour lines are plotted. Comparing the -20.0 volt contour lines shows that in all cases these lines were fairly coincident. Since the -20.0 volt contour is fairly close to the sheath boundary (Fig. 7) a tentative conclusion may be drawn. Namely, that to a fair approximation the screen hole sheath boundary has the same position and shape for any screen-to-accelerator grid separation ratio when the grid set is operated at its minimum beam divergence condition. This result supports earlier observations[3,6,7] which indicated that the minimum ion beam divergence angle occurred at approximately the same normalized perveance per hole value irrespective of the screen-to-accelerator separation distance. Another feature of interest in Fig. 11 is that more plasma ions are directed away from the screen grid webbing and through the screen hole as the screen-to-accelerator grid separation ratio is reduced. This effect is illustrated by the electric field vectors shown in Fig. 11. Deflection of plasma ions away from the screen grid webbing and through the screen hole as the grid separation is reduced would lead to increased maximum normalized perveance per hole values. Such an increase has been observed previously.[6]

Effect of Discharge Chamber Parameters

Tests were conducted to determine what effect discharge voltage, plasma electron temperature and primary-to-Maxwellian electron density
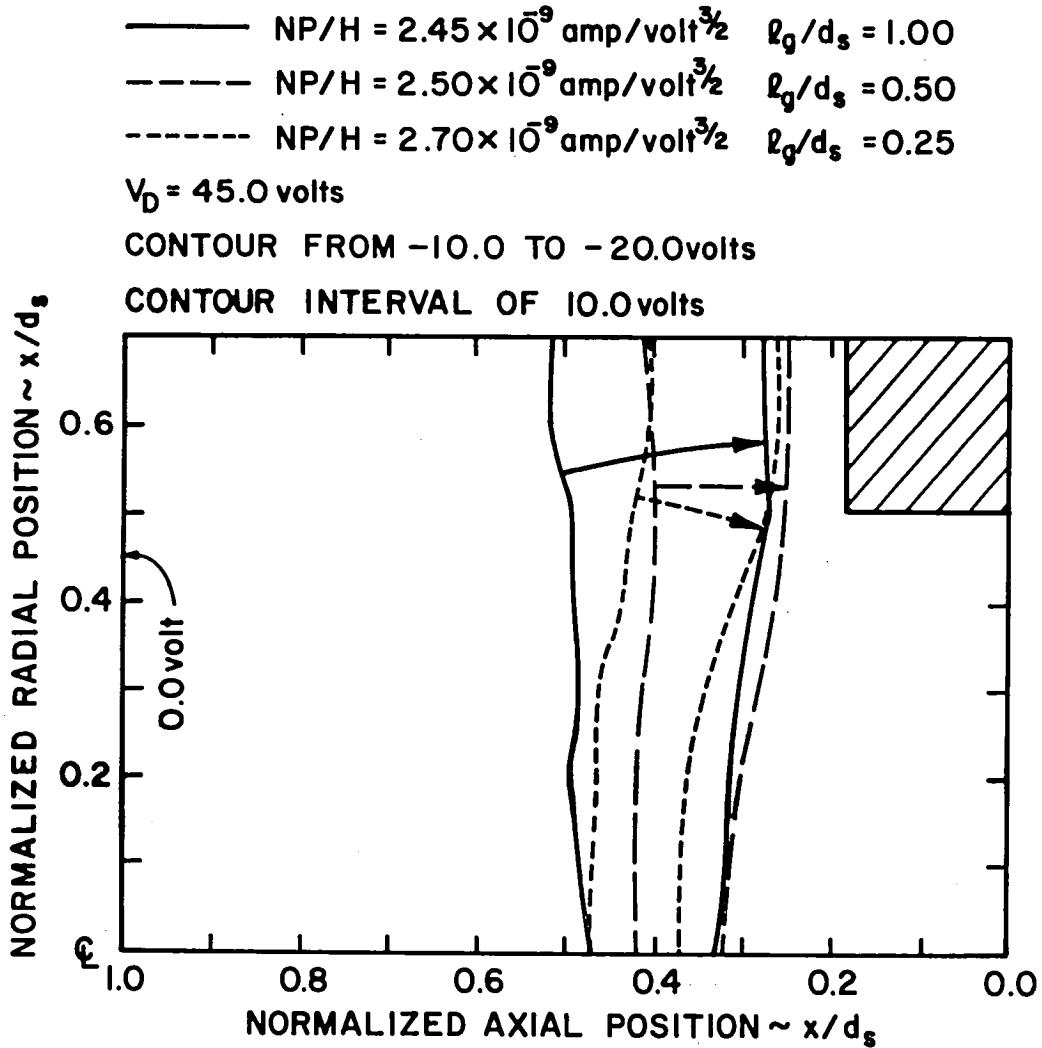
Fig. 11 Screen hole sheath movement and shape change with decreasing screen-to-accelerator grid separation, $\frac{\ell_g}{d_s}$, (half sheath profile).

ratio variations had on the screen hole plasma sheath characteristics. Figure 12 shows the results of these tests. Here, Fig. 12a depicts a half sheath profile for the standard grid set at typical operating conditions. Figures 12b and 12c show this same standard grid set operating at a higher discharge voltage and bell jar pressure respectively. In Figures 12b and 12c the sheath boundary was defined as that location where the local electron density was about 10% of the bulk plasma electron density, (the determination of screen hole sheath electron density is presented in a later section). This definition was consistant with that used to define the sheath boundary in Fig. 12a. Comparing Figs. 12a and 12b it is evident that the sheath potential contours have similar shapes. However, the sheath boundary for a discharge voltage of 65.0 volts is positioned farther from the screen grid than the standard 45.0 volt discharge voltage condition of Fig. 12a. This displacement is non-uniform, with the sheath boundary adjacent to the screen grid webbing having been moved by a greater amount than the boundary position along the screen hole center line. Such a sheath movement with increasing discharge voltage, had been theorized by Kaufman.[20] The argument being that adjacent to the screen grid webbing the plasma is shielding itself from a potential drop of the order of the discharge voltage. While, along the screen hole axis, the plasma is shielding itself from a potential drop of the order of the total accelerating voltage (Fig. 1) of which the discharge voltage is only a small fraction. Consequently, discharge voltage variations do not alter the total accelerating voltage significantly. Therefore, the plasma feels the accelerator system potential drop relatively unchanged and the sheath boundary is only slightly altered accordingly.
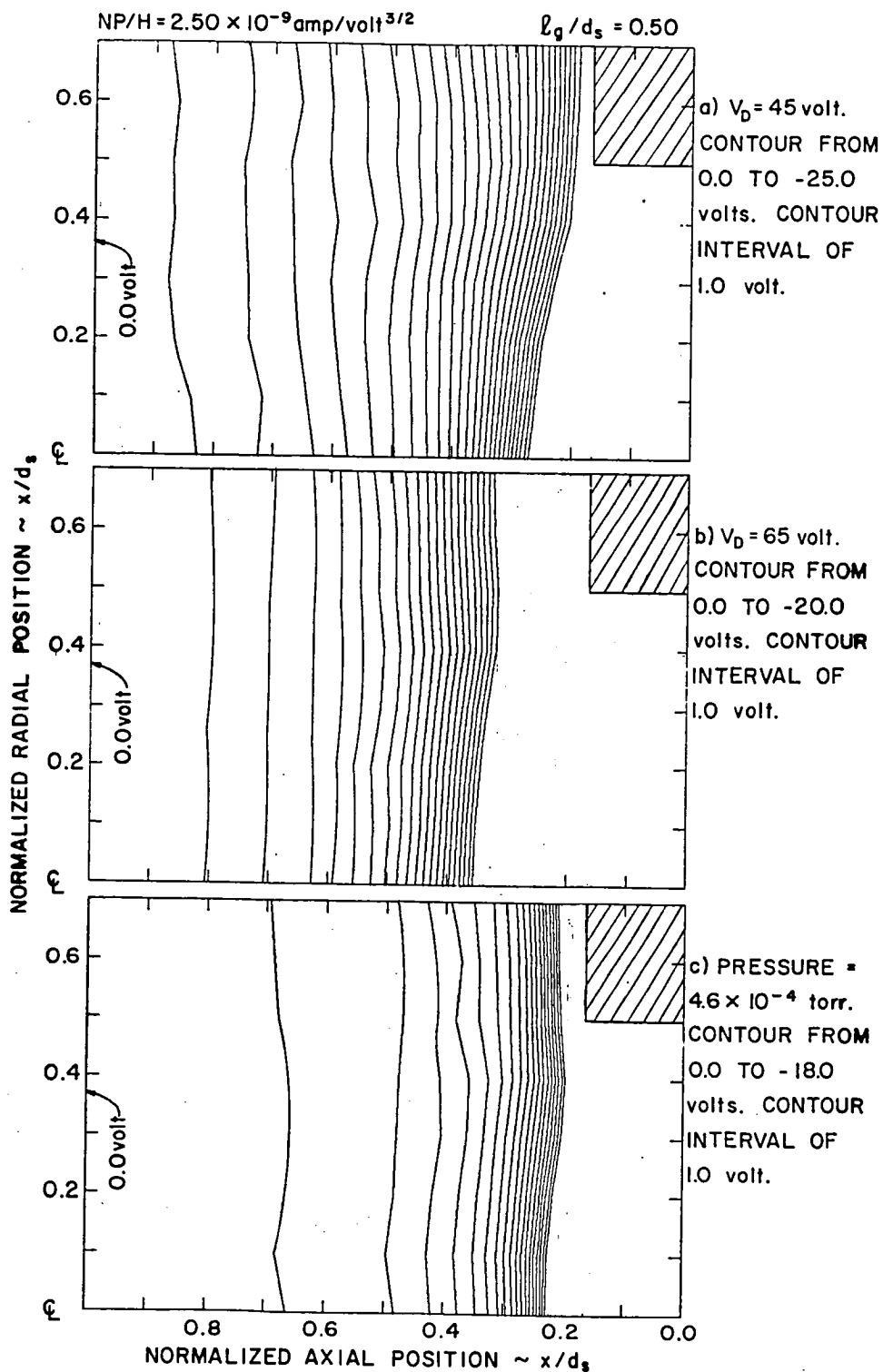
Fig. 12 Comparison of sheath half profile for standard grid set geometry and operating conditions (a), with sheath half profile for increased discharge voltage (b), and increased ion source operating pressure (c).

Of interest is to note that the sheath boundary shape associated with the high discharge voltage condition of Fig. 12b yields ion beam divergence angles lower by about 10% than those obtained at the standard operating condition of Fig. 12a.[6] It is believed that these lower ion divergence angles are a consequence of the sheath boundary being less bowed for the high discharge voltage than the boundary associated with operation at a lower discharge voltage. This would mean that those ions emerging from the periphery of the sheath boundary in Fig. 12b would have smaller off-axis ion velocity components giving lower ion beam divergence angles than the ions emerging from the more bowed sheath boundary of Fig. 12a. Another interesting feature of Fig. 12b is that the sheath potential profiles adjacent to the screen grid webbing are quite flat and parallel the webbing surface. Consequently, no plasma ions are directed away from the screen grid webbing in this case. This is in contrast to operation at a lower discharge voltage, as shown in Fig. 12a. Here, the sheath potential contours adjacent to the screen grid webbing do direct some of the plasma ions away from the webbing surface and through the screen hole where they add to the extracted ion current. Figures 12a and 12b suggest that operation at a higher discharge voltage should result in lower maximum normalized perveance per hole values. This observation supports the result of earlier experiments[6] that showed higher normalized perveance per hole values were possible when the discharge voltage was decreased.

Figure 12c shows the effect of increasing the bell jar background argon pressure by a factor of two over that used to obtain the results of Fig. 12a. From Fig. 12c it is evident that this pressure increase has reduced substantially the screen hole plasma sheath thickness.

With this large increase in neutral argon number density, the small
spherical probe used to measure bulk plasma properties (Appendix A) in-
dicated that the primary-to-Maxwellian electron density ratio was approx-
imately zero as compared to approximately 0.20 for the standard pressure
condition of Fig. 12a, while the Maxwellian electron temperature was
only slightly lower for the high pressure condition. It is believed
that this near absence of primary electrons, with essentially only low
energy Maxwellian electrons present, was responsible for the relative
bunching of potential lines shown in Fig. 12c compared to those of
Fig. 12a. Such a sheath thickness reduction would be expected to occur
because the lower energy Maxwellian electrons would not penetrate far in-
to the sheath. Consequently, the sheath potential gradients would be
steeper. Figure 12c shows also that the sheath boundary for a high neutral
argon number density has approximately the same position and shape as
that associated with the standard operating condition (Fig. 12a). This
similarity supports earlier work that showed only slight ion beam divergence
changes with argon gas flow, or bell jar pressure, variations.[6]

Effect of Screen Grid Thickness

Screen grid thickness variations had a pronounced effect on the
screen hole plasma sheath adjacent to the screen grid webbing.
Figure 13 provides physical insight into these effects by showing how
the screen hole plasma sheath moves as the screen grid thickness is
varied. Over the central portion of the screen hole the plasma feels
the negative accelerator grid potential most strongly; screen grid
thickness and hence screen potential distribution changes have little
effect in this region. Conversely, adjacent to the screen grid webbing
the plasma sets up a potential distribution such that an equal ion and
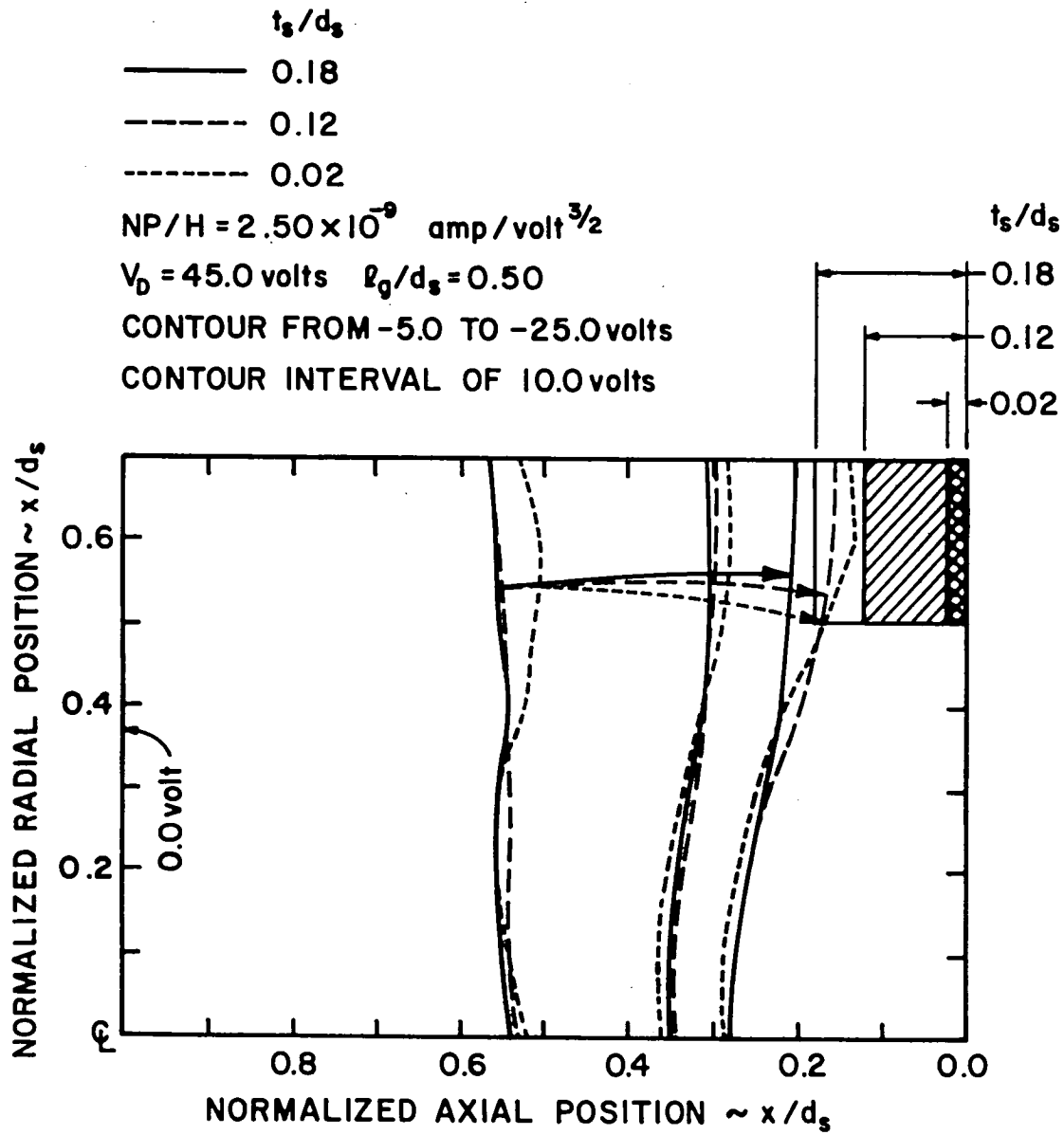
Fig. 13 Effect of screen grid thickness variations, $\dfrac{t_s}{d_s}$, on the screen hole sheath shape and position (half sheath profile).

electron flux arrive at the webbing surface. This latter effect is a surface phenomenom only and is not dependent on the screen grid thickness. As the screen grid thickness is reduced, the plasma sheath boundary remains essentially fixed in position along the screen hole axis while adjacent to the webbing the sheath boundary follows the receding screen grid surface. However, with decreasing screen grid thickness the negative accelerator grid potential is felt more strongly at the periphery of the screen hole. This tends to retard the downstream motion of the plasma ions and electrons after the receding screen grid in this region. The net result of these two competing effects is that eventually a limiting screen grid thickness is reached such that further thickness reductions do not alter appreciably the screen grid webbing sheath boundary position or shape. Although not shown in Fig. 13, other screen grid thicknesses were examined also. These tests indicated a limiting screen grid thickness ratio, t_s/d_s, of ~ 0.05.

Figure 13 shows that the motion of the sheath boundary after the receding screen grid surface gives rise to a sheath potential distribution at the screen grid webbing which tends to direct plasma ions away from the webbing and through the screen hole as screen grid thickness is reduced. This focusing effect is illustrated graphically by electric field vectors in Fig. 13. It should be noted that these ion trajectory vectors are similar to those presented in Fig. 11. Indeed, the web focusing effect evident in Fig. 11 was a consequence of physical processes similar to those described above. Except that in Fig. 11, decreasing grid separation rather than decreasing screen grid thickness, resulted in the enhanced communication between the negative accelerator grid potential and discharge plasma at the screen hole perhiphery.

The arguments presented previously indicate that the position of the central portion of the screen hole plasma sheath would remain essentially unaltered with screen grid thickness changes. This behavior is verified in Fig. 14 where screen hole sheath profiles are compared for a very thick screen grid (t_s/d_s = 0.49) and a conventional thin screen grid (t_s/d_s = 0.18). Figure 14 shows that a plasma sheath has formed adjacent to the upstream surface of the thick screen grid webbing, but that the position of the central portion of the screen hole plasma sheath is still controlled by the negative accelerator grid potential and is relatively unchanged. The sheath probes shape, Fig. 4a, prevented the probe from entering very far into the screen hole and this is why only a portion of the -15.0 volt contour line and no -25.0 volt contour line is shown in Fig. 14, however, the trend is clear. Examination of the sheath potential contours adjacent to the very thick screen grid webbing indicates that ions from within the screen hole could easily intercept the inner screen hole surface and recombine. Indeed, the normalized perveance per hole value indicated in Fig. 14, while only about 65% of the maximum value to be expected for the conventional thin screen grid (Fig. 2), corresponded to the maximum obtainable normalized perveance per hole for the very thick screen grid.

The web focusing effect illustrated in Figs. 13 and 14 indicates that increased beam currents and decreased discharge chamber plasma losses (or increased beam ion production efficiencies) could be expected for screen grid thickness reductions. The trend of increased beam current, or normalized perveance per hole, has been observed previously for thin screen grids.[3,6,21]
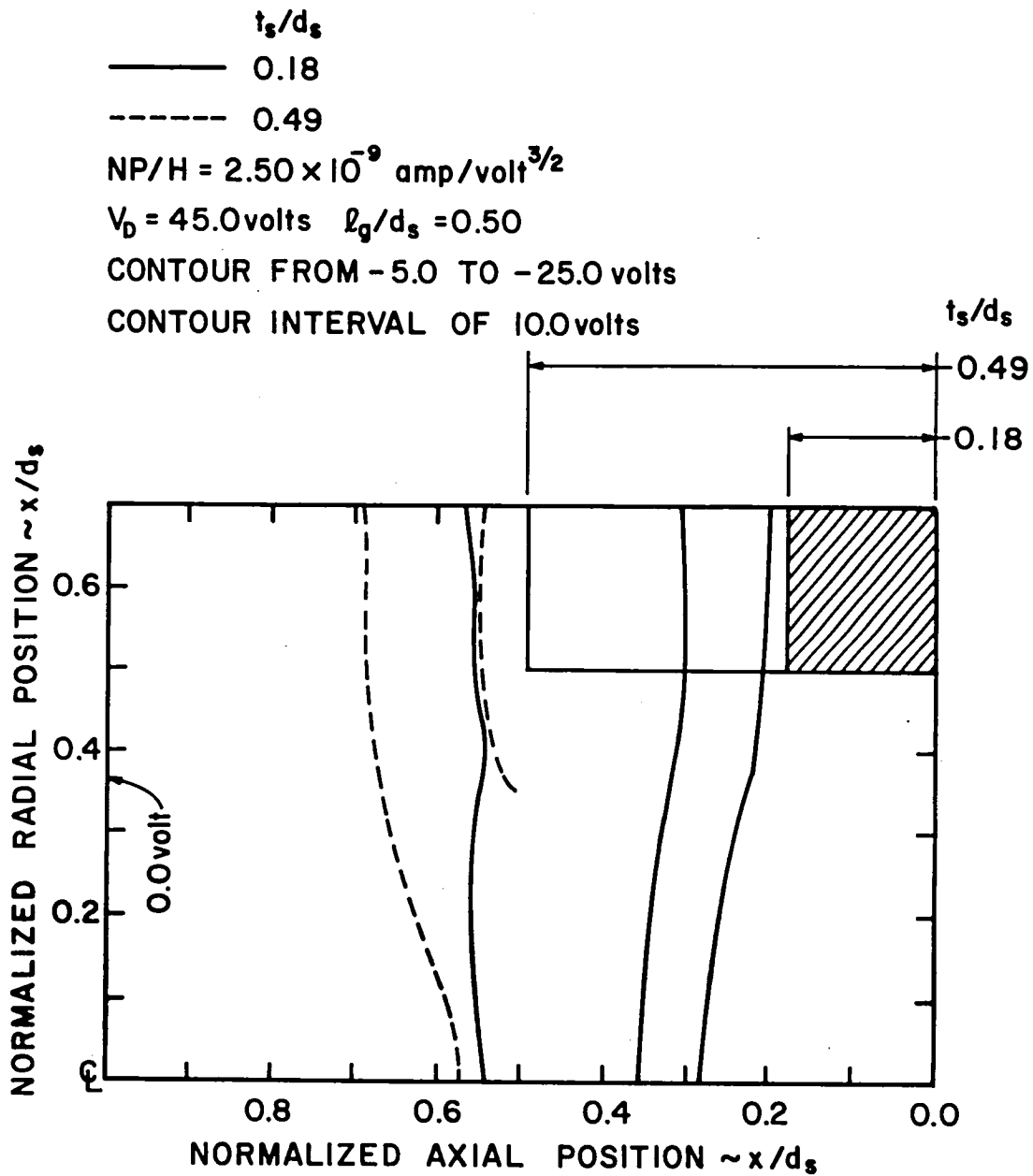
Fig. 14 Effect of thick screen grid (large $\frac{t_s}{d_s}$) on sheath position and shape (half sheath profile).

The different levels of ion recombination on the screen grid would be expected to be associated with different discharge loss* levels. Figure 15 shows a plot of discharge loss, normalized to the discharge loss value for t_s/d_s = 0.49, against screen grid thickness (the screen hole diameter d_s was held constant at 12.7 mm). This curve illustrates dramatically the adverse screen web focusing effect introduced with increasing screen grid thickness.

The results presented in Figs. 13-15 are clear evidence that ion impingement on the screen grid webbing decreases significantly with screen grid thickness reductions. This has obvious implications for decreased screen grid sputter erosion and increased accelerator system lifetime (a parameter of critical importance in ion thrusters[22]) as the screen grid thickness is reduced. In fact, it appears that an effort to thicken the screen grid to give longer erosion life may accelerate the erosion effect. Of course there are definite, but perhaps not insurmountable problems in fabricating screen grids of the thicknesses suggested in Figs. 13-15. Also, without some sort of comparative erosion life test being conducted the lifetime conclusions presented here are tentative only.

Effect of Screen Hole Shaping

Numerous workers[1,2,5,19,23] have reported conflicting results as to the effect shaping the screen grid holes has on beam current and ion beam divergence. In order to further the understanding of the effects

---

*
The parameter, discharge loss, is a measure of the beam ion production efficiency and gives a quantitative estimate of the energy (in eV) necessary to produce one beam ion.

$$\text{DISCHARGE LOSS} = \frac{V_D \times I_D}{J_B} \sim eV/ion$$

V_D = DISCHARGE VOLTAGE
I_D = DISCHARGE CURRENT
J_B = BEAM CURRENT
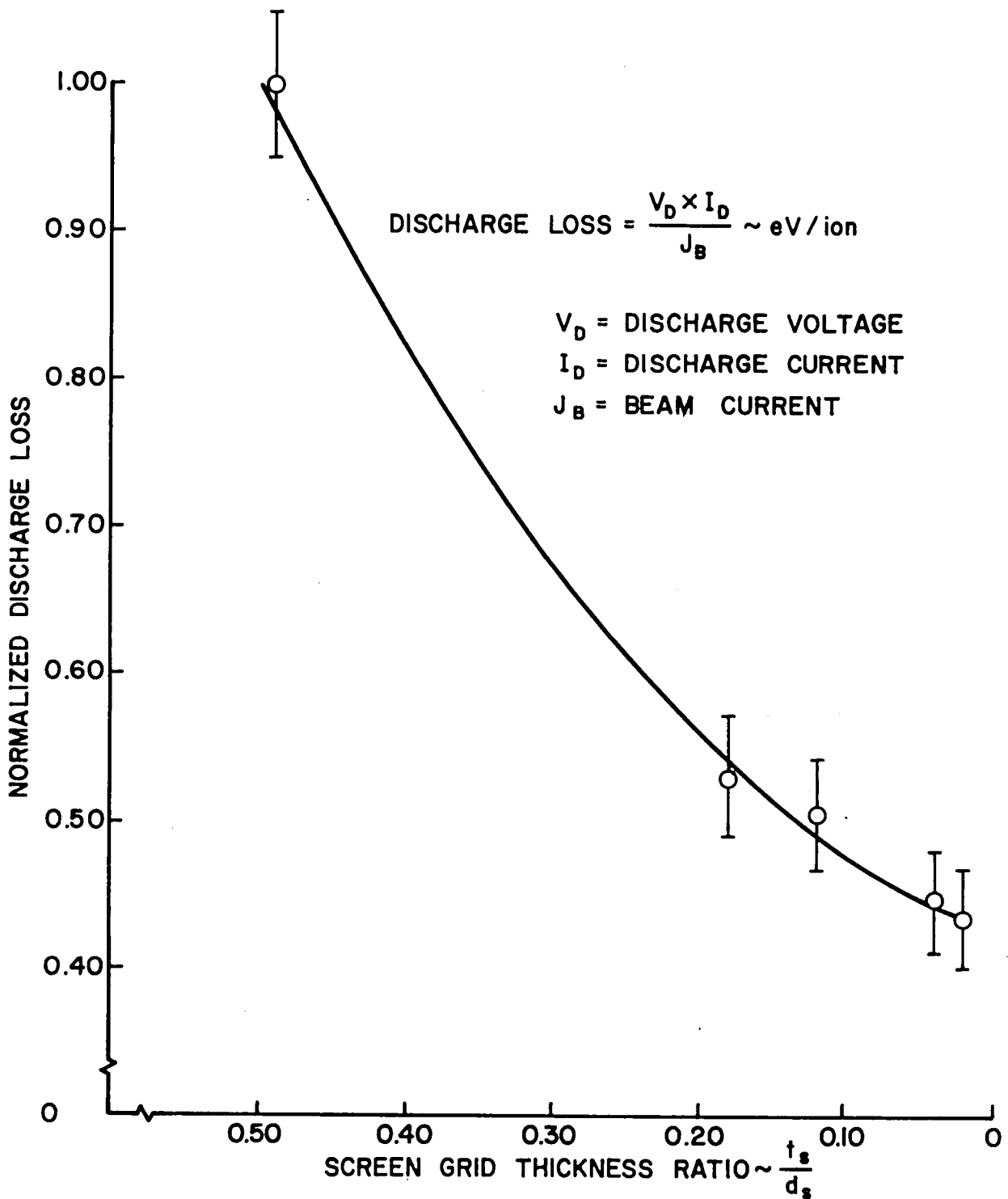
Fig. 15 Detrimental effect of large screen grid thickness ratios, $\frac{t_s}{d_s}$, on discharge loss (or plasma ion production efficiency).

of screen hole shape changes the screen hole plasma sheaths of variously

shaped screen holes were examined experimentally.

It was found that putting a 41° chamfer on the upstream (discharge

plasma) screen hole face had only a very slight effect on the screen

hole plasma sheath potential contours. Similarly, no change from the un-

chamfered screen grid geometry was observed in the discharge loss level

and maximum obtainable normalized perveance per hole. This null result

supports earlier evidence by Kerslake and Pawlik[23] that screen grid hole

chamfering is of little if any merit.

Some workers[1,5] have reported computer solutions and experimental

results which indicate that counterboring the downstream screen hole

face leads to significant screen hole sheath shape changes with lower

divergence angles and increased beam current. Such a modification was

made to the tapered screen grid discussed above. Figure 16 compares

screen hole sheath profiles for this chamfered and counterbored screen

grid to those of a conventional cylindrical screen hole geometry. Only

slight differences in the sheath potential contours are observed. At

the screen grid webbing the potential contours are fairly coincident.

Towards the screen hole center more differences are apparent and the

sheath boundary for the chamfered and counterbored screen hole (dashed

-25.0 volt contour in Fig. 16) is displaced upstream slightly relative

to the cylindrical screen hole sheath boundary.

One would expect that by counterboring the screen hole the

effective hole diameter has been enlarged. Such an enlargement must

decrease slightly the positive potential that the screen grid webbing

can impress at the screen hole center. Consequently, what shielding

effect the screen grid could interpose between the discharge plasma and

—— CONVENTIONAL SCREEN GRID

---- CHAMFERED AND COUNTER BORED
     SCREEN GRID

$NP/H = 2.50 \times 10^{-9}$ amp/volt$^{3/2}$

$V_D = 45.0$ volts $\ell_g/d_s = 0.50$

CONTOUR FROM -5.0 TO -25.0 volts

CONTOUR INTERVAL OF 10.0 volts

$t_s/d_s = 0.18$

NORMALIZED RADIAL POSITION $\sim x/d_s$

0.6

0.4

0.2

0.0 volt

NORMALIZED AXIAL POSITION $\sim x/d_s$

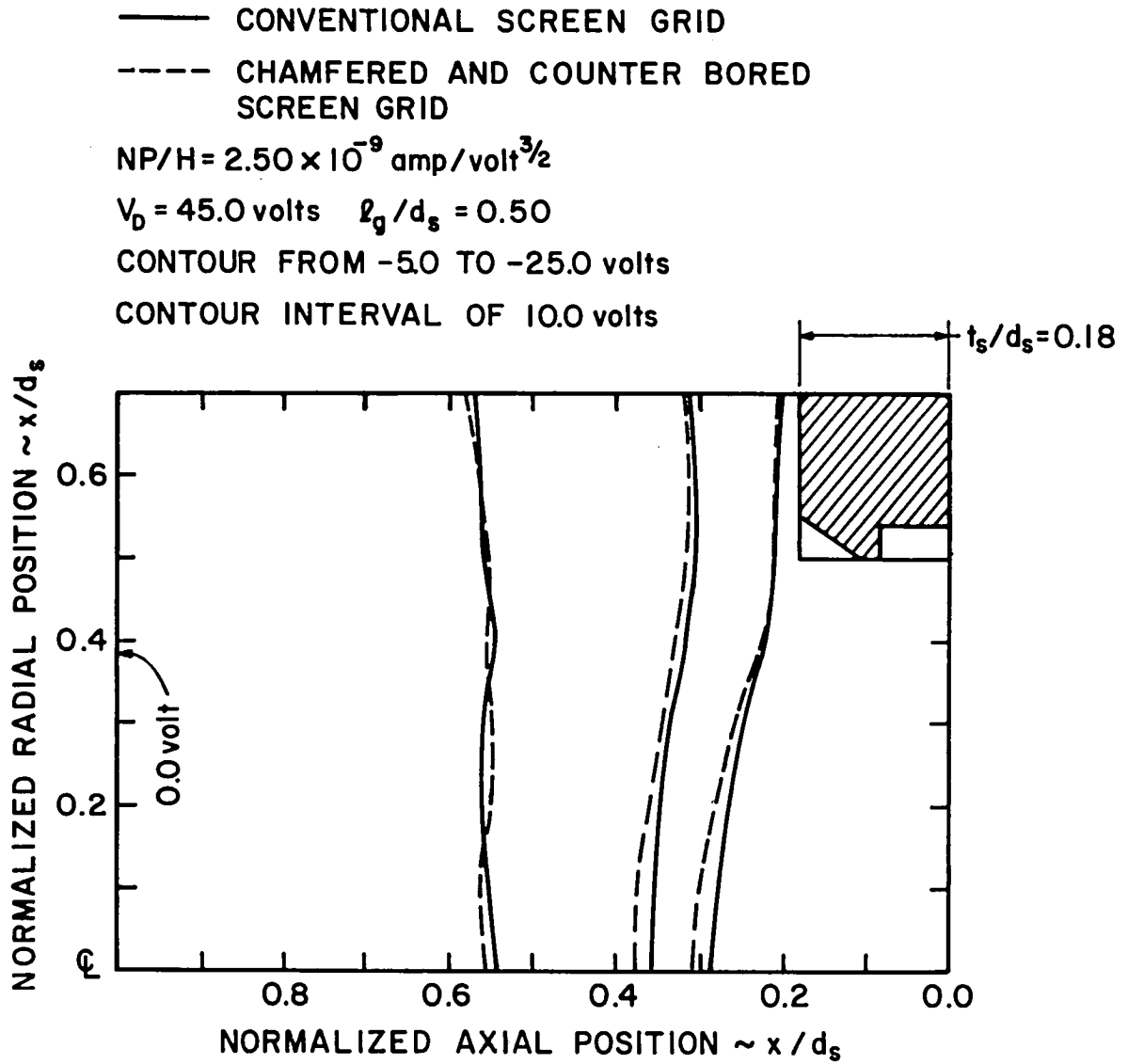0.8   0.6   0.4   0.2   0.0

Fig. 16   Effect of screen hole shape changes on sheath
position and shape (half sheath profile).

negative accelerator grid will have been reduced. As a result, the plasma electrons would see a stronger retarding electric field as they approached the central portion of the screen hole. This stronger retarding field would prevent plasma electrons from penetrating through the ion acceleration region to a depth possible with the cylindrical hole geometry. The net effect would be to move the central portion of the screen hole sheath boundary slightly upstream, as is shown in Fig. 16. This trend agrees qualitatively with the previously mentioned computer solution predictions although it is much less pronounced than these solutions predict.

The chamfered and counterbored screen grid shown in Fig. 16 gave a slight decrease in discharge loss (<3%) and a slight decrease in the maximum obtainable beam current (<3%) compared to similar parameters recorded for the cylindrical hole geometry. No ion beam divergence data were obtained for any shaped screen hole geometry. Also, direct accelerator grid impingement currents could not be measured accurately because of the relatively high facility background pressure ($\sim$2 x 10^{-4} torr). However, the slight screen hole plasma sheath shape and position changes apparent in Fig. 16 suggest beam divergence and direct ion impingement variations would be small as the screen hole shape was altered for thin screen grids.

It is felt that the discrepancy between the results of the screen hole shaping tests presented here and those presented elsewhere[1,2,5,19] lies in the screen grid thicknesses considered. As pointed out previously, the screen hole plasma sheath is within the screen hole for large values of the screen grid thickness ratio only (Fig. 14). With the sheath inside the screen hole, it appears more likely that screen

hole shape changes would have a significant effect on the ensuing ion trajectories. References 1, 2, 5 and 19 all dealt with thick screen grids and large values of the screen grid thickness ratio t_s/d_s. In most cases these thick screen grids were a consequence of mechanical and thermal load requirements. From Figs. 13-15 it is evident that large screen grid thickness ratios must result in large ion source and screen grid thermal loads. It appears, then, that the degree of optimization for the accelerator systems studied in Refs. 1, 2, 5 and 19 was significantly poorer than those typical of most ion thruster applications; where thin screen grids are used. However, as evidenced from Figs. 13-15, even typical ion thruster accelerator systems (where $t_s/d_s \sim 0.18$) are operating at higher than necessary discharge losses, if structural requirements are ignored.

Experimental and Theoretical Comparison

Figure 17 compares the screen hole plasma sheath obtained theoretically by Kaufman,[4] using the space-charge-flow computer program of Bogart and Richley,[24] against the sheath boundary (-25.0 volt contour line) obtained experimentally at the same grid geometry and operating conditions. Qualitatively, the sheath boundaries are similar but their positions are different. In the theoretical approach of Bogart and Richley the screen hole plasma sheath was defined as a single equipotential surface at screen grid potential across which the electric field was set equal to zero. Consequently, the sheath obtained theoretically is represented as a discontinuity separating the discharge plasma from the region of accelerated ions, with the sheath terminating on the screen hole edge. This model was successful in predicting qualitatively many

$NP/H = 3.00 \times 10^{-9}$ amp/volt$^{3/2}$

$V_T = 500$ volt $\quad R = 0.7$

$\ell_g/d_s = 0.33 \quad d_a/d_s = 1.00$
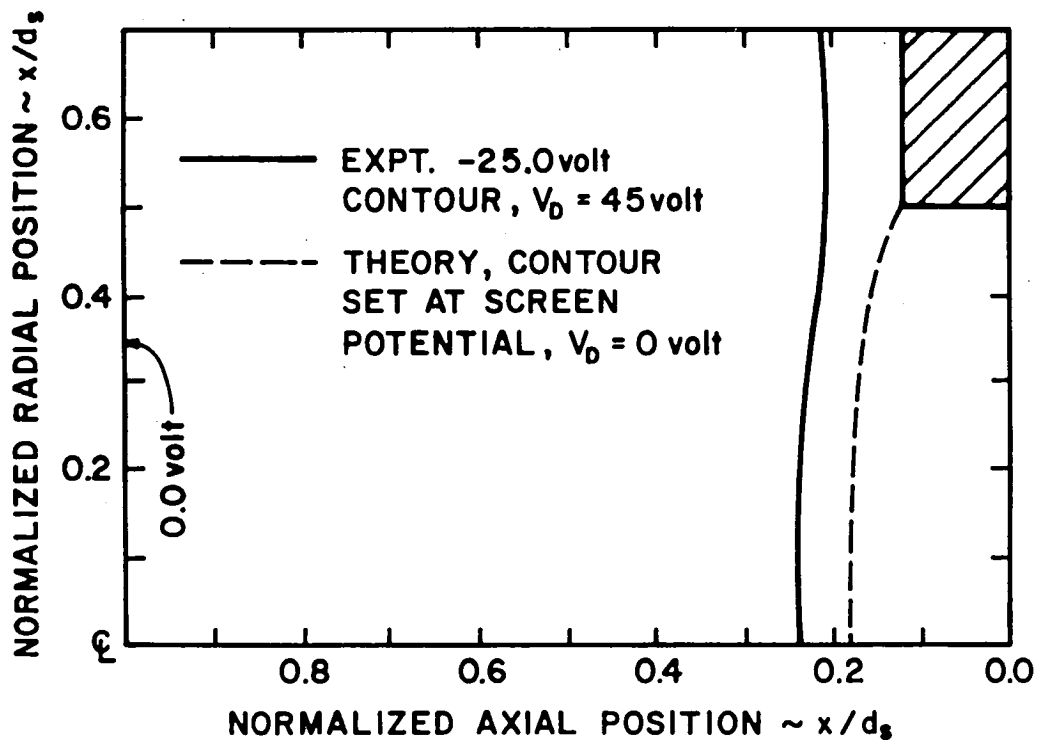
$t_s/d_s = 0.12 \quad t_a/d_s = 0.33$

Fig. 17 Comparison of experimental and theoretical sheath potential contours (half sheath profile).

ion beam divergence effects.[4] However, the present experimental investigation indicates that the screen web focusing effects, screen hole sheath thickness and potential distributions are very important to a complete understanding of the ion extraction process. It is felt that the inability of the theoretical sheath model of Bogart and Richley to account for these effects is responsible for the poor quantitative agreement betweeen theoretical ion beam divergence results[4] and those obtained experimentally in previous studies.[6,7]

Other, more rigorous, theoretical sheath models have been pursued but each has its own inherent difficulties and necessary approximations. Whealton et. al.[25] have listed the shortcomings of these various models while presenting the case for their own theoretical treatment, which is perhaps the most sophisticated model to date. The screen hole plasma sheath position and shape predictions obtained with this model agree qualitatively with some of the results of this study. However, the published results were for a large screen grid thickness ratio and it is not known how well the Whealton model could predict the screen web focusing effects found characteristic of thinner screen grids. Ion beam divergence predictions obtained with the Whealton model are contained in Refs. 5 and 25. These results contain a fair amount of scatter but do show trends qualitatively similar to those recorded by other workers.[1,2,3,4,6,7] The accuracy with which the ion beam divergence data contained in Refs. 6 and 7 were obtained, coupled with the broad range of ion accelerator systems investigated and the success that has been achieved by applying the results of this work,[26] suggest that it should serve as the yardstick against which theoretical model predictions are measured. Similarly, the screen hole plasma sheath characteristics

presented and discussed in this section appear to define the important physical processes governing ion extraction from a discharge plasma. As such, these results should serve as a standard of comparison for those approximations of most validity in future screen hole plasma sheath models.

SCREEN HOLE SHEATH CORRELATIONS

Sheath Plasma Density Variation

In the previous section, the screen hole plasma sheath was charac-
terized by a set of equipotential contours. These contours defined the
extent over which the plasma was perturbed by the accelerator system
potentials and were very useful in estimating initial ion trajectories.
Also useful is an understanding of the effect sheath potential gradients
have on the local ion and electron densities. This information can be
obtained directly from the sheath potential contours and the bulk plasma
conditions. Briefly, a one-dimensional model was developed incorporating
Poisson's equation, the ion energy equation and conservation of ion flux.
The ions were assumed to enter the collisionless sheath region with the
modified Bohm velocity developed by Masek.[16,27] The second derivative
of the potential with respect to distance was obtained numerically
through the sheath from the experimental data. Using this as input to
the model, it was possible to calculate the ion and electron density
variation through the sheath. Appendix D details the development of
this model.

Figure 18 shows a plot of the ion and electron density variation
through the centerline of the screen hole plasma sheath of the standard
grid set at typical operating conditions (Fig. 8). The ion and elec-
tron densities have been normalized with respect to their value a
distance of one screen hole diameter back from the origin. The data
presented in Fig. 18 were taken with two separate, but identically con-
structed, sheath probes separated by a two month time period. What
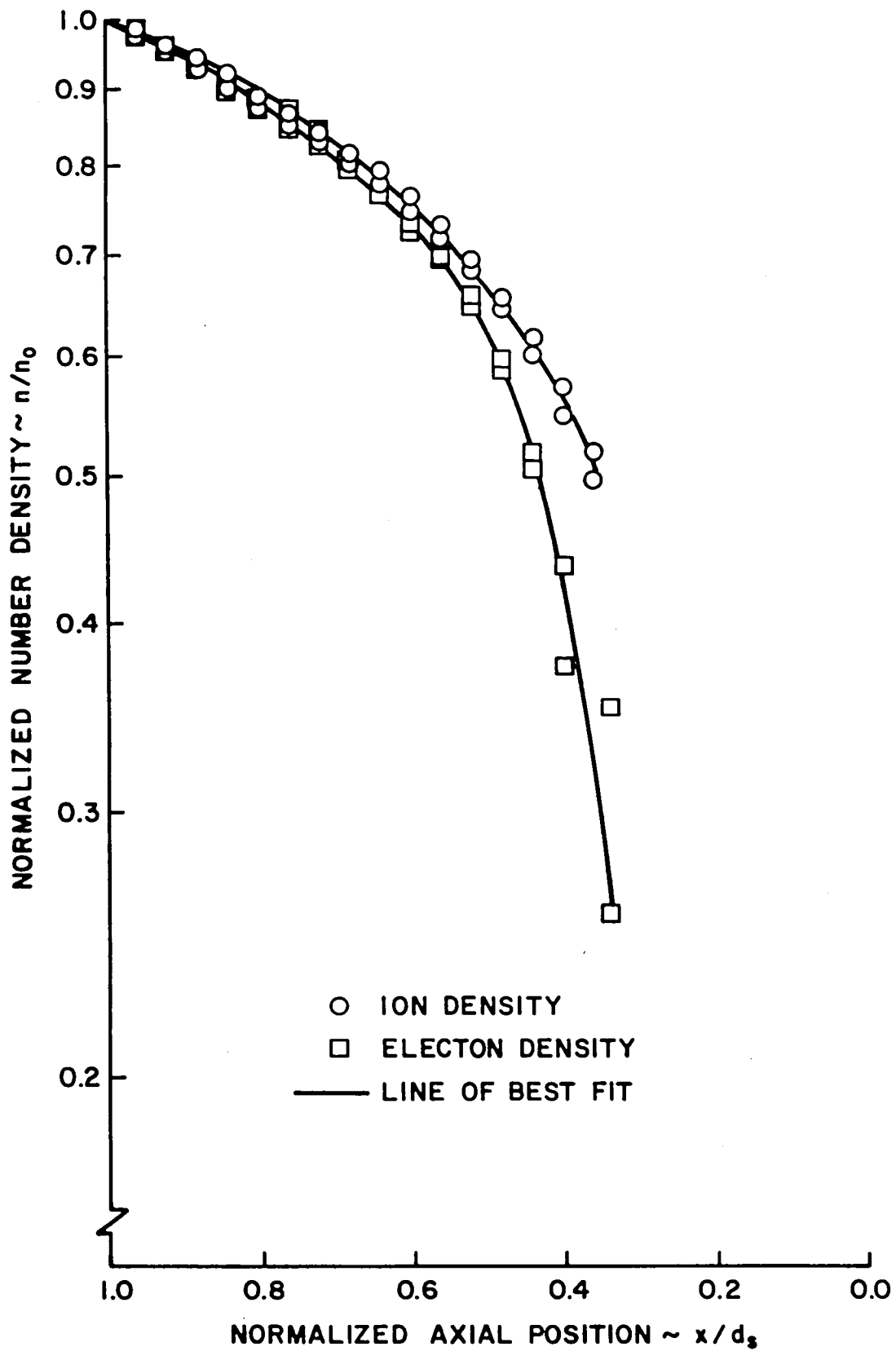scatter is evident is believed to be a function of the extreme

Fig. 18 Ion and electron density variation through a

screen hole plasma sheath.

sensitivity in taking the second derivative of the sheath potential variation, rather than any inherent experimental inconsistancy. In fact, the sheath potential contours obtained with the different probes were virtually identical. Figure 18 shows clearly how the plasma ion density drops off slowly, as the ions are accelerated through the sheath, while in contrast, the plasma electron density drops off much more rapidly due to the retarding field seen by the electrons. It should be noted that, to the author's knowledge, Fig. 18 contains the first experimental plot of the ion and electron density variation through any plasma sheath. Some work was done by Goldan[28] in the late 1960's on determining sheath potential variations using an electron beam probing method. However, he examined the sheath adjacent to a planar electrode and could only sense potential gradients an order of magnitude less than those detected during this experiment.

Characteristically, all theoretical plasma sheath models assume a Maxwell-Boltzmann distribution of electron densities in the sheath region of the form

$$n_e = n_o \exp(\frac{V}{T}) \tag{1}$$

where V is the potential in the sheath and is negative, being set equal to zero in the bulk plasma, while n_o and T are the electron density and temperature (in eV) in the bulk plasma. In reality, the plasma electron population in most discharges is comprised of a Maxwellian and primary electron energy contribution.[13,14]

To test the validity of Eq. (1), the normalized electron density and sheath potential variation for the standard grid set geometry were plotted on a semi-log scale. Figure 19 shows the results of this plotting procedure. Here, the circled data points are for the standard
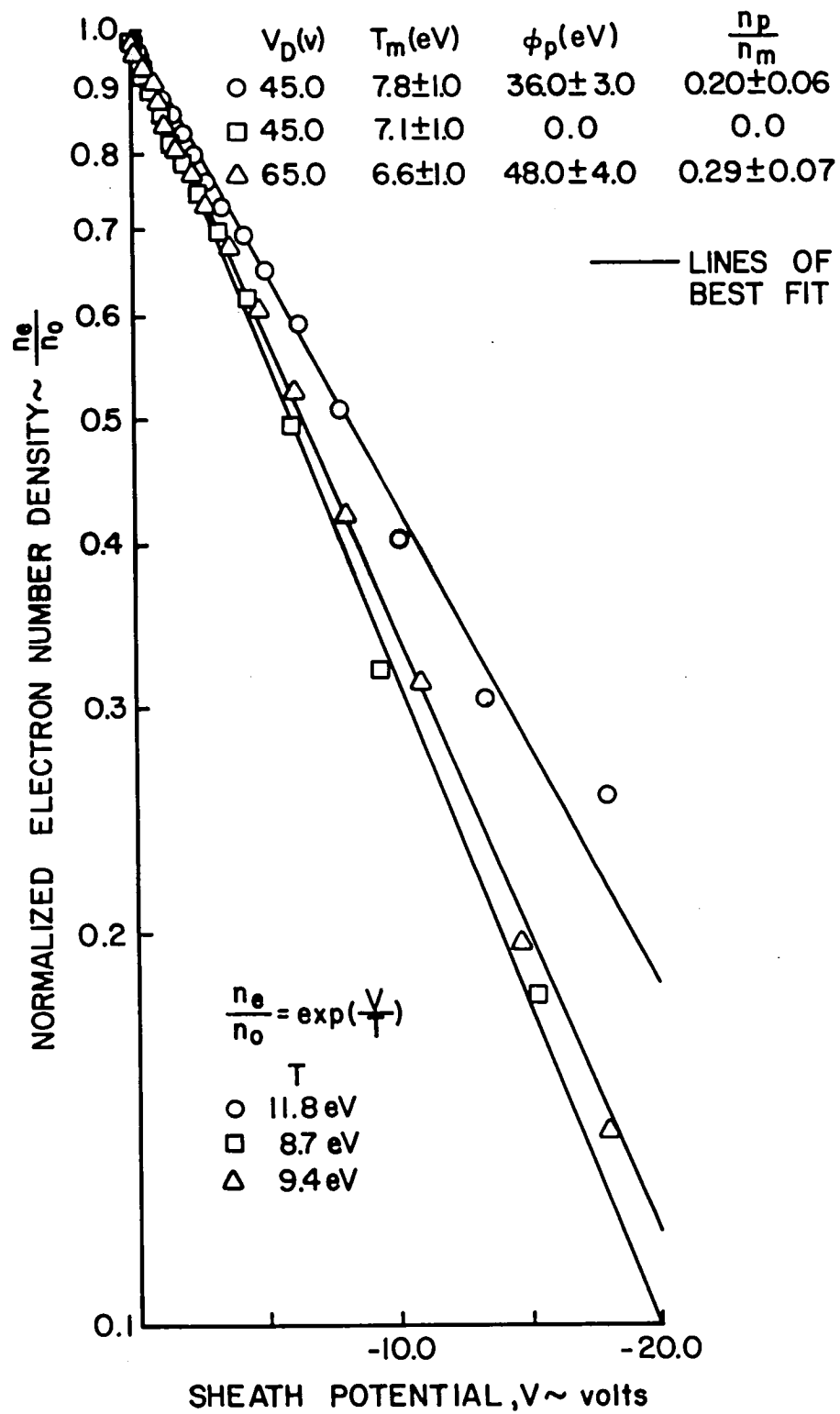
Fig. 19 Variation of electron density and potential through the screen hole sheath.

grid set geometry at typical operating conditions, the squares are for the same grid set geometry but twice the bell jar pressure (so that essentially only Maxwellian electrons were present), while the triangles are for grid set operation at a higher discharge voltage. These three operating conditions are the same as those discussed previously in Fig. 12. It is the normalized electron density versus sheath potential along the screen hole axis for the three sheath profiles of Fig. 12 that is being plotted in Fig. 19. From Fig. 19 it appears that the Boltzmann, or Barametric, equation (Eq. (1)) is a reasonable approximation to the observed functional form of the sheath electron density and potential variation. The effective electron temperatures determined from the slope of the lines of best fit, are consistant with the variations in the Maxwellian electron temperatures (T_M), primary electron energies (ϕ_p) and the ratio of primary-to-Maxwellian electron densities (n_p/n_m) of the different operating conditions. Calculations were made to determine if the effective electron temperature T, could be expressed quantitatively as a function of T_M, ϕ_p and n_m/n_p. No successful correlations were obtained. It was felt that knowledge of the electron energy distribution function in the bulk plasma might yield an estimate of this effective temperature. However, this parameter is difficult to obtain experimentally and was beyond the scope of this work.

In summary, the results contained in Fig. 19 are experimental verification of the validity of the Boltzmann, or Barametric, equation (Eq. (1)) for the description of electron densities in a plasma sheath. Self,[29] has commented on the range of applicability of Eq. (1) in a plasma sheath and these results support his theoretical predictions that any departure from Eq. (1) would be small. Although only the

electron density variation along the sheath axis has been presented in Fig. 19, similar results were also obtained for the electron density variation in the sheath adjacent to the screen grid webbing.

Effective Screen Hole Sheath Area

A method to determine an effective screen hole sheath area, as well as check the consistancy of the entire experiment can be accomplished by the following argument.

Consider the ion current density equation given below

$$j = n_i v_i e \tag{2}$$

where j is the ion current density entering a screen hole, n_i and v_i are the ion density and ion velocity at any point through the screen hole sheath and e is the electronic charge. Setting A_s as the effective screen hole sheath ion extraction area and making use of the modified Bohm velocity developed by Masek[16,27] results in

$$J = n_0 e A_s [\frac{KT_m}{M_i} (1 + \frac{n_p}{n_m})]^{\frac{1}{2}} . \tag{3}$$

Here, J is the ion current per screen hole, n_0 is the plasma density at the screen hole sheath entrance, T_m and n_p/n_m are the Maxwellian electron temperature and the primary to Maxwellian electron density ratio respectively, while K and M_i are the Boltzmann constant and ion mass.

Everything in Eq. (3) may be obtained experimentally except the effective screen hole sheath area A_s, consequently, this parameter can be solved for directly. Numerous calculations were performed whereby the effective sheath area A_s was determined for a range of grid geometry and accelerator system operating conditions. The cumulative

experimental error associated with those measurable parameters in Eq. (3) prevented very accurate sheath area differences and trends to be obtained. However, for operating conditions where the screen hole plasma sheath had not entered the screen hole, application of Eq. (3) yielded effective screen hole sheath areas consistantly larger than the screen aperture area by not more than 20%. This result supports the observations of the previous section which clearly showed ion trajectories leaving a sheath boundary whose area was, in general, greater than the screen hole area. Perhaps the importance of the reasonable agreement between the calculated effective screen hole sheath area and that expected from the observed sheath potential contours is that the applicability of Eq. (3) has been substantiated. Inherent in the derivation of Eqs. (2) and (3) are the assumptions that the ion motion towards the screen hole plasma sheath is predominately one-dimensional with these ions assuming the modified Bohm velocity of Masek at the sheath entrance. These assumptions appear validated by the results discussed here.

CONCLUDING REMARKS

Results of the first comprehensive experimental investigation of the physical processes governing ion extraction from a plasma have been presented. The screen hole plasma sheath (the transition region wherein significant ion acceleration and complete electron retardation occurs) has been defined successfully by equipotential plots for a variety of ion accelerator system geometries and operating conditions. These potential contours have shown that the screen hole plasma sheath extends over a large distance, influencing ion and electron trajectories significantly at least fifteen Debye lengths within the discharge chamber. The electron density variation within the screen hole plasma sheath satisfied a Maxwell-Boltzmann density distribution (i.e., the Barometric equation) at an effective electron temperature dependent on the discharge plasma primary to Maxwellian electron density ratio. Similarly, plasma ion flow up to and through the sheath was predominately one-dimensional and the ions entered the sheath region with a modified Bohm velocity. Only at large values of the screen grid thickness ratio did the screen hole plasma sheath enter the screen hole. However, a significant screen webbing ion focusing effect indicated poor plasma generation efficiency and low extracted ion currents with large values of the screen grid thickness ratio.

The results of this work define those parameters of most importance to the ion extraction process from a plasma. It is hoped that the development of successful theoretical ion extraction and focusing models might be aided by the physical insight embodied within this work.

APPENDIX A

THICK SHEATH SPHERICAL PROBE ANALYSIS

The small spherical Langmuir probe used to measure discharge plasma properties is shown in Fig. A-1a. Plasma conditions in the ion source discharge chamber used for the screen hole sheath study were such that the Debye length (the charged particle shielding distance) at typical operating conditions was 0.5 mm or greater. This large Debye length necessitated the use of a thick sheath probe analysis. A typical spherical probe trace is shown in Fig. A-1b. This probe trace was analyzed in the following way.

In the retarding region the electron current to the probe was made up of thermalized electrons in a Maxwellian energy distribution and unthermalized primary electrons of energy near the plasma discharge voltage. This electron energy distribution has been studied by Martin[13] for an argon discharge. From Beattie[14] the electron current to the probe in the retarding region of the probe trace shown in Fig. A-1b is given by

$$I = B_1 + B_2 V + B_3 \exp(B_4 V). \qquad (A-1)$$

Here, the primary electron current is the linear portion while the exponential portion pertains to the Maxwellian electron current. A non-linear least squares fit technique was used to fit Eq. (A-1) to the retarding portion of the probe trace depicted in Fig. A-1b. This procedure was a computer library routine and converged rapidly to give the coefficients B_1, B_2, B_3 and B_4. With B_1 and B_2 known the straight line primary electron current contribution was subtracted off the entire
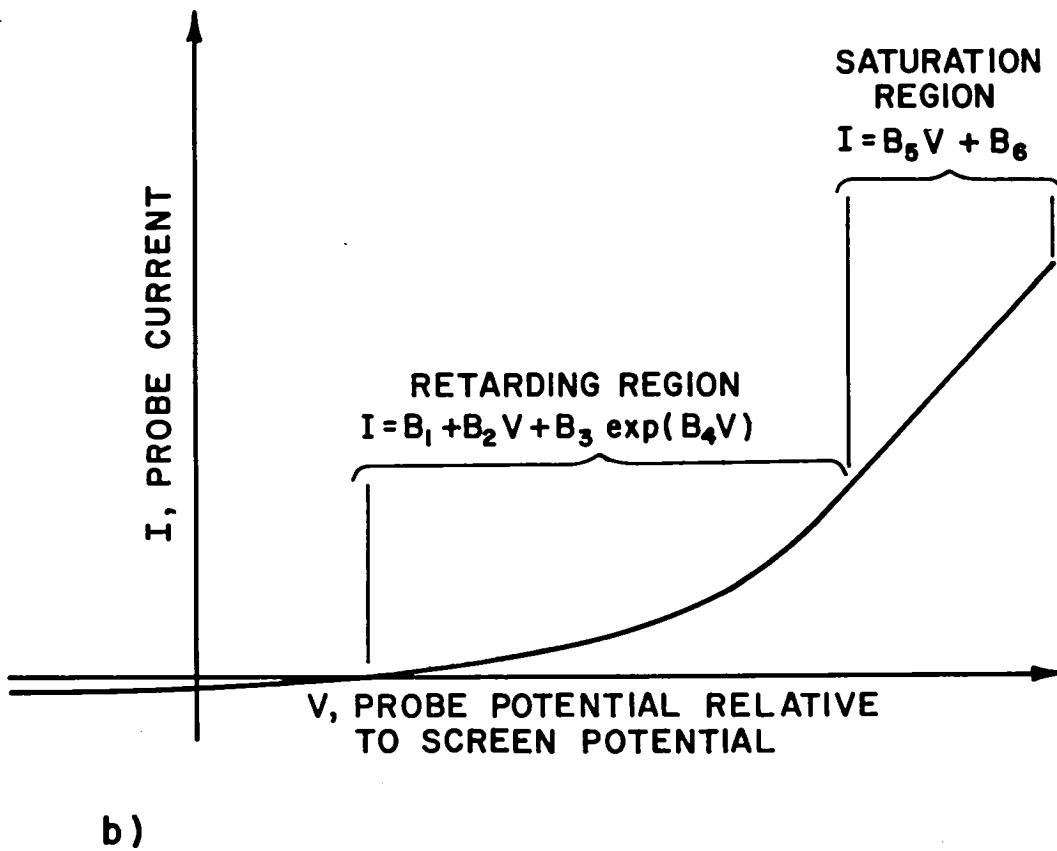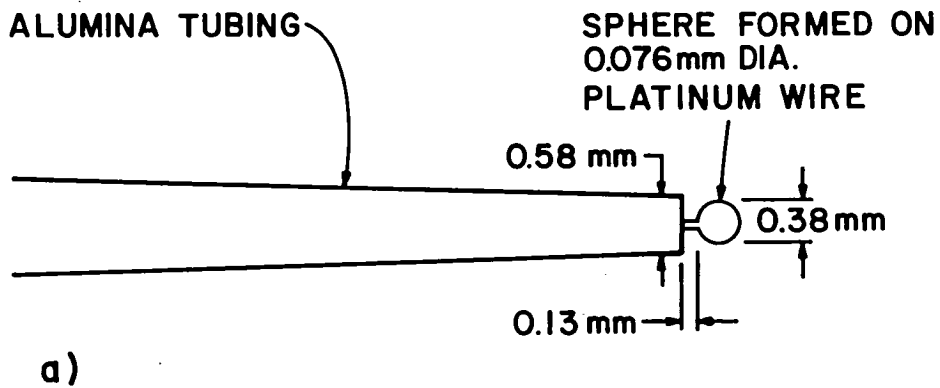
a)

b)

Fig. A-1   (a)   Spherical Langmuir probe design details.

(b)   Typical thick sheath spherical Langmuir probe trace.

Langmuir probe characteristic shown in Fig. A-1b. The equation to the electron retarding region now described Maxwellian electrons only and became

$$Ln\ I = LnB_3 + B_4\ V.\qquad\text{(A-2)}$$

Also, the Maxwellian electron current in the saturation region of the probe trace is, for a thick sheath spherical probe,[15]

$$I = B_5\ V + B_6\ .\qquad\text{(A-3)}$$

Where B_5 is the slope of the electron saturation region shown in Fig. A-1b after the linear primary electron current contribution has been subtracted off the probe trace. The magnitude of this slope is related to the conductance of the plasma. Similarly, B_6 may be obtained by solving Eq. (A-3) at any current-voltage point in the Maxwellian electron saturation region. Substituting Eq. (A-3) into Eq. (A-2) gives

$$I = (B_6 - \frac{B_5}{B_4}\ Ln\ B_3) + \frac{B_5}{B_4}\ Ln\ I\ .\qquad\text{(A-4)}$$

Equation (A-4) was solved iteratively to obtain the Maxwellian electron saturation current I_{sat} and then either Eq. (A-2) or (A-3) was used to evaluate the plasma potential V_p. Where I_{sat} and V_p are the current and voltage values at that critical point in the Langmuir probe trace where plasma electrons are neither retarded or attracted by the probe. Using these results plus the inverse of coefficient B_4 (which is the Maxwellian electron temperature T_m in eV) the electron density n_e was determined using the following equations.[15] In the retarding region:

$$n_e = 2.969 \times 10^{12} - \frac{I_{sat}}{r_p^2\ \sqrt{T_m}}\ m^{-3}\ .\qquad\text{(A-5)}$$

In the saturation region:

$$n_e = 2.969 \times 10^{12} \cdot B_5 \cdot \frac{\sqrt{T_m}}{r_p^2} \; m^{-3} \; . \qquad (A-6)$$

Here, r_p is the spherical probe radius in meters. The electron density values computed from Eqs. (A-5) and (A-6) agreed within 20% consistantly. The average of both values was used to determine discharge plasma electron and ion densities. Also, the ratio of primary to Maxwellian electron number density n_p/n_m was evaluated for each probe trace. The equation used in this determination is given below[14]

$$\frac{n_p}{n_m} = \frac{2}{\sqrt{\pi}} \left(\frac{T_m}{V_p + B_1/B_2} \right)^{\frac{1}{2}} \frac{I_{prim}}{I_{sat}} \; . \qquad (A-7)$$

Where I_{prim} is the primary electron current reaching the probe at plasma potential and was calculated by using the linear portion of Eq. (A-1). While the quantity, $V_p + B_1/B_2$, is equal to the primary electron energy, ϕ_p in eV.

APPENDIX B

SHEATH PROBE ERROR

An emissive Langmuir probe has been used in the screen hole plasma sheath study. When surrounded by a plasma, and with the filament heated to incandescence, an emissive probe will float at a potential near the local potential of the surrounding plasma. The error, or the difference between the emissive probe floating potential and plasma potential is the result of two effects. The first is the potential variation along the hot filament wire because of the ohmic heating voltage drop. For this experiment a carefully balanced D.C. battery supply was used to heat the filament. The voltage drop along the length of exposed heated filament has been estimated to be the order of 0.5 volt. The second source of error is due to the formation of a double sheath around the floating probe. This double sheath is a direct consequence of having more electrons produced by the hot filament than are needed to satisfy the requirement of zero net current between the floating probe and plasma. A quantitative estimate of the voltage drop in this double sheath is the purpose of this appendix.

For this analysis the simplified case of an infinite planar electron emitter is considered and the analysis is one-dimensional. The filament is floating and assumed to emit more electrons than necessary to satisfy the zero net current requirement (this represents a condition of operation typical of the emissive probe used in the screen hole plasma sheath study). The double sheath thus formed is shown as follows.
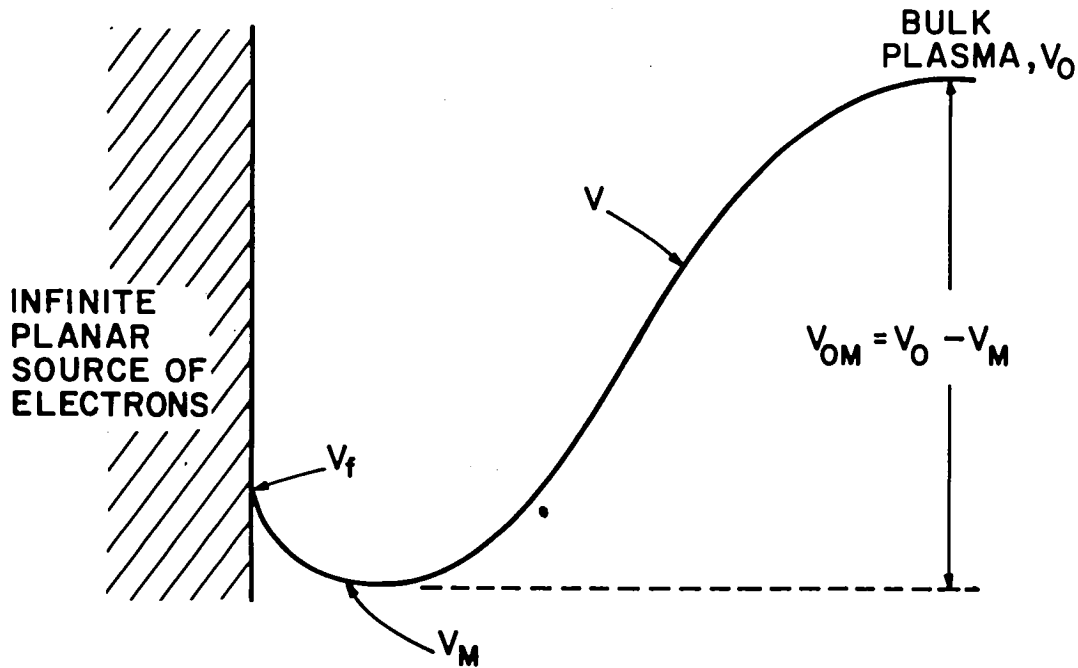
Define: V_o = Plasma potential.

V_f = Planar filament floating potential.

V_M = Double sheath potential minimum.

V = Potential at any point between filament and plasma.

ρ_{o_i} = Bulk plasma ion charge density.

ρ_{o_e} = Bulk plasma electron charge density.

ρ_{o_f} = Filament electron charge density at filament surface.

ρ_i, ρ_e, ρ_f = Plasma ion, electron and filament electron charge density at location where potential is V.

ρ_M, ρ_{eM}, ρ_{fM} = Plasma ion, electron and filament electron charge density at $V = V_M$.

To estimate the potential difference V_{om} it is necessary to solve Poissons' equation, which in one-dimensional form is:

$$\frac{d^2V}{dx^2} = -\frac{\rho}{\varepsilon_o}$$

Multiplying both sides by dV/dx and integrating with respect to X gives

$$\left(\frac{dV}{dx}\right)^2 = -\frac{2}{\varepsilon_0} \int \rho dV + C_1 \ .$$

At the double sheath boundaries the voltage gradient is zero. This leads to the boundary conditions:

$$\left.\frac{dV}{dx}\right|_{V=V_0} = 0 \quad , \quad \left.\frac{dV}{dx}\right|_{V=V_m} = 0 \ .$$

Applying these boundary conditions to the equation above yields

$$\int_{V_M}^{V_0} \rho dV = 0 \ . \tag{B-1}$$

Also, since the planar filament is floating, the net current between the filament and bulk plasma must be zero at any point. Examining the currents that must be present at the double sheath potential minimum results in the following equation:

$$\rho_{fM} v_{fM} + \rho_{iM} v_{iM} = \rho_{eM} v_{eM} \tag{B-2}$$

where v_{fM}, v_{iM} and v_{eM} are the velocities of the filament electrons and plasma ions and electrons at the potential minimum.

Equations (B-1) and (B-2) need now to be solved simultaneously to obtain the potential difference V_{0M}. First, Eq. (B-1) is constructed piecemeal by considering each of the species present.

Plasma Ions

The plasma ions are assumed to enter the double sheath region from the plasma with the Bohm velocity,[16] since no primary electrons are being considered. These ions are accelerated as they travel from V_0 to V_M and are retarded slightly as they go from V_M to V_f. Restricting

ourselves to the accelerating region only, the ion energy equation can be written as follows:

$$\frac{1}{2} kT_M = \frac{1}{2} m_i\, v_i^2 - e(V_0 - V)$$

where T_M is the temperature of the Maxwellian plasma electrons and v_i is the ion velocity at any point between V_0 and V_M. Re-arranging gives:

$$v_i = \left[\frac{kT_M}{m_i} + \frac{2e}{m_i} (V_0 - V) \right]^{\frac{1}{2}}.$$

From conservation of ion current a second equation is obtained

$$\rho_{oi} \left(\frac{kT_M}{m_i} \right)^{\frac{1}{2}} = \rho_i\, v_i .$$

Substituting the above form of v_i gives:

$$\rho_i = \rho_{oi} \left[1 + \frac{2e}{kT_M} (V_0 - V) \right]^{-\frac{1}{2}}.$$

Integrating this expression with respect to V gives

$$\int_{V_m}^{V_0} \rho_i\, dV = \int_{V_m}^{V_0} \rho_{oi} \left[1 + \frac{2e}{kT_M} (V_0 - V) \right]^{-\frac{1}{2}} dV$$

setting

$$t^2 = 1 + \frac{2e}{kT_M} (V_0 - V) \quad \text{and} \quad dV = - \frac{kT_M}{e} t\, dt$$

and noting that when

$$V = V_0 , \quad t = 1$$

and when

$$V = V_M , \quad t = \left[1 + \frac{2e}{kT_M} (V_0 - V_M) \right]^{\frac{1}{2}}.$$

one obtains

$$\int_{V_M}^{V_0} \rho_i\, dV = - \frac{kT_M}{e} \rho_{oi} \int_{\left[1 + \frac{2e}{kT_M} (V_0 - V_M) \right]^{\frac{1}{2}}}^{1} dt$$

or
$$\int_{V_M}^{V_0} \rho_i dV = \frac{kT_M}{e} \rho_{oi} \left\{ [1 + \frac{2e}{kT_m} V_{oM}]^{\frac{1}{2}} - 1 \right\} . \qquad (B-3)$$

Plasma Electrons

Electrons from the plasma see a potential hill as they enter the region between V_0 and V_M and are retarded. This potential hill, as viewed by the plasma electrons, is shown below.
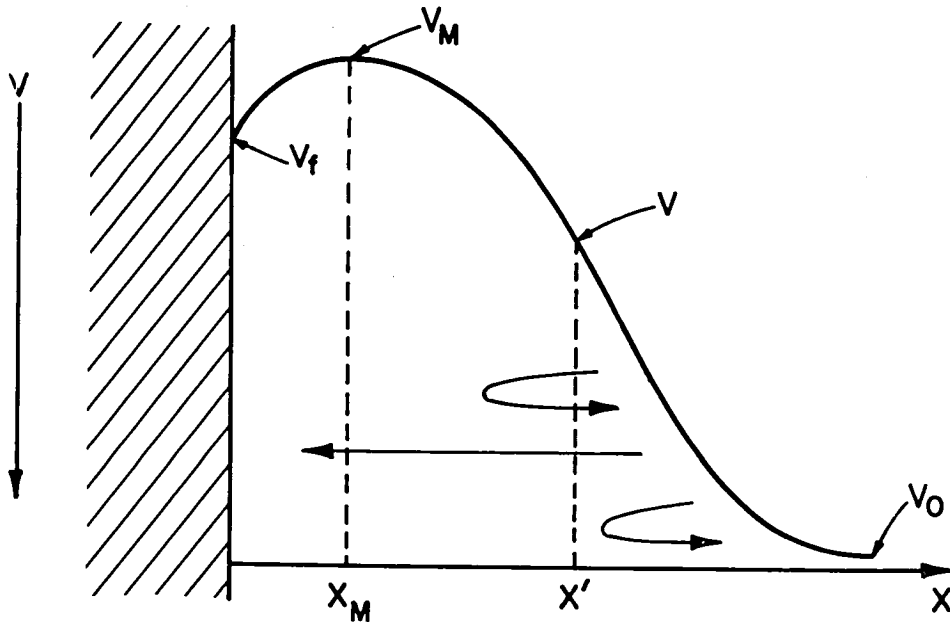
Consider some point x' lying between V_0 and V_M. The plasma electron space charge at x' is due to two electron velocity groups. Plasma electrons with initial velocities between $[\frac{2e}{M_e} (V_0-V)]^{\frac{1}{2}}$ and $[\frac{2e}{M_e} (V_0-V_M)]^{\frac{1}{2}}$ reach and go past x', are reflected back from the potential hill and pass through x' again on their way back into the plasma. Hence, these electrons contribute twice to the electron space charge at x'.[17] Also those electrons with initial velocity between $[\frac{2e}{M_e} (V_0-V_M)]^{\frac{1}{2}}$ and ∞ pass

through x' and contribute to the charge density at this point. But these electrons cross over the potential hill V_M and never return to the plasma. The plasma electron charge density at x' then takes the following form.

$$\rho_e = 2\rho_{oe} \int_{[\frac{2e}{M_e}(V_o-V)]^{\frac{1}{2}}}^{[\frac{2e}{M_e}(V_o-V_M)]^{\frac{1}{2}}} f(v_{oe})dv_{oe} + \rho_{oe} \int_{[\frac{2e}{M_e}(V_o-V_M)]^{\frac{1}{2}}}^{\infty} f(v_{oe})dv_{oe}$$

Here, $f(v_{oe})$ represents the one-dimensional Maxwellian velocity distribution of the plasma electrons in the plasma. Where:

$$f(v_{oe}) = \left(\frac{M_e}{2\pi kT_M}\right)^{\frac{1}{2}} \exp\left(\frac{-M_e v_{oe}^2}{2kT_M}\right) \quad .$$

This distribution can be written in terms of the Maxwellian distribution at any velocity v_e by making use of the plasma electron energy equation:

$$\frac{1}{2} M_e v_{oe}^2 = \frac{1}{2} M_e v_e^2 + e(V_o-V) \quad .$$

Substituting back gives:

$$f(v_e) = \left(\frac{M_e}{2\pi kT_m}\right)^{\frac{1}{2}} \exp\left(\frac{-M_e v_e^2}{2kT_M}\right) \exp\left(\frac{-e(V_o-V)}{kT_M}\right) \quad .$$

The limits of integration of the equation defining ρ_e must be changed also. Substituting $v_{oe}^2 = \frac{2e}{M_e}(V_o-V)$ into the preceeding energy equation gives:

$$e(V_o-V) = \frac{1}{2} M_e v_e^2 + e(V_o-V)$$

or

$$v_e = 0 \quad .$$

Similarly, substituting $v_{oe}^2 = \frac{2e}{M_e}(V_o - V_M)$ into this energy equation gives:

$$e(V_o - V_M) = \frac{1}{2} M_e v_e^2 + e(V_o - V)$$

or

$$v_e^2 = \frac{2e}{M_e}(V - V_M) .$$

Hence, the expression for ρ_e becomes:

$$\rho_e = \rho_{oe} \left(\frac{M_e}{2\pi k T_M}\right)^{\frac{1}{2}} \exp\left[\frac{-e(V_o - V)}{k T_M}\right] \left[2 \int_0^{[\frac{2e}{M_e}(V-V_M)]^{\frac{1}{2}}} \exp \frac{-M_e v_e^2}{2k T_M} \, dv_e + \int_{[\frac{2e}{M_e}(V-V_M)]^{\frac{1}{2}}}^{\infty} \exp \frac{-M_e v_e^2}{2k T_M} \, dv_e \right] .$$

One can now set $t = \left(\frac{M_e}{2k T_M}\right)^{\frac{1}{2}} v_e$ and $dt = \left(\frac{M_e}{2k T_M}\right)^{\frac{1}{2}} dv_e$

and note that $v_e = \left[\frac{2e}{M_e}(V - V_M)\right]^{\frac{1}{2}}$

corresponds to $t = \left[\frac{e}{k T_M}(V - V_M)\right]^{\frac{1}{2}} .$

Substituting these results back into ρ_e yields:

$$\rho_e = \rho_{oe} \left(\frac{M_e}{2\pi k T_M}\right)^{\frac{1}{2}} \exp\left(\frac{-e(V_o - V)}{k T_M}\right)\left(\frac{2k T_M}{M_e}\right)^{\frac{1}{2}} \left[2 \int_0^{[\frac{e}{k T_M}(V-V_M)]^{\frac{1}{2}}} \exp(-t^2)dt + \int_{[\frac{e}{k T_M}(V-V_M)]^{\frac{1}{2}}}^{\infty} \exp(-t^2)dt \right]$$

But, $\int_0^x \exp(-t^2)dt = \frac{\pi^{\frac{1}{2}}}{2} \operatorname{erf}(x)$

and $\int_x^{\infty} \exp(-t)dt = \frac{\pi^{\frac{1}{2}}}{2} [1 - \operatorname{erf}(x)]$

therefore

$$\rho_e = \rho_{oe} \exp\left(\frac{-e(V_0-V)}{kT_M}\right)\left[\mathrm{erf}\left[\frac{e}{kT_M}(V-V_M)\right]^{\frac{1}{2}} + \frac{1}{2}\left(1-\mathrm{erf}\left[\frac{e}{kT_M}(V-V_M)\right]^{\frac{1}{2}}\right)\right]$$

$$\rho_e = \frac{1}{2}\rho_{oe} \exp\left(\frac{-e(V_0-V)}{kT_M}\right)\left[1+\mathrm{erf}\left[\frac{e}{kT_M}(V-V_M)\right]^{\frac{1}{2}}\right] \ .$$

Integrating this expression with respect to V gives

$$\int_{V_M}^{V_0} \rho_e dV = \frac{1}{2}\rho_{oe} \int_{V_M}^{V_0} \exp\left(\frac{-e(V_0-V)}{kT_M}\right)\left[1 + \mathrm{erf}\left[\frac{e}{kT_M}(V-V_M)^{\frac{1}{2}}\right]\right]dV \ .$$

Unfortunately this integral is too cumbersome to be evaluated with ease analytically, if at all. However, it may be approximated fairly accurately by the use of Simpsons' three point rule. The result is given below:

$$\int_{V_M}^{V_0} \rho_e dV = \frac{1}{12}\rho_{oe} V_{OM}\left[\exp\left(\frac{-eV_{OM}}{kT_M}\right) + 1 + \mathrm{erf}\left(\frac{eV_{OM}}{kT_M}\right)^{\frac{1}{2}}\right.$$

$$\left. + 4 \exp\left(\frac{-eV_{OM}}{2kT_M}\right)\left[1 + \mathrm{erf}\left(\frac{eV_{OM}}{2kT_M}\right)^{\frac{1}{2}}\right]\right] \ . \tag{B-4}$$

Filament Electrons

Electrons from the filament see a potential hill as they leave the filament.
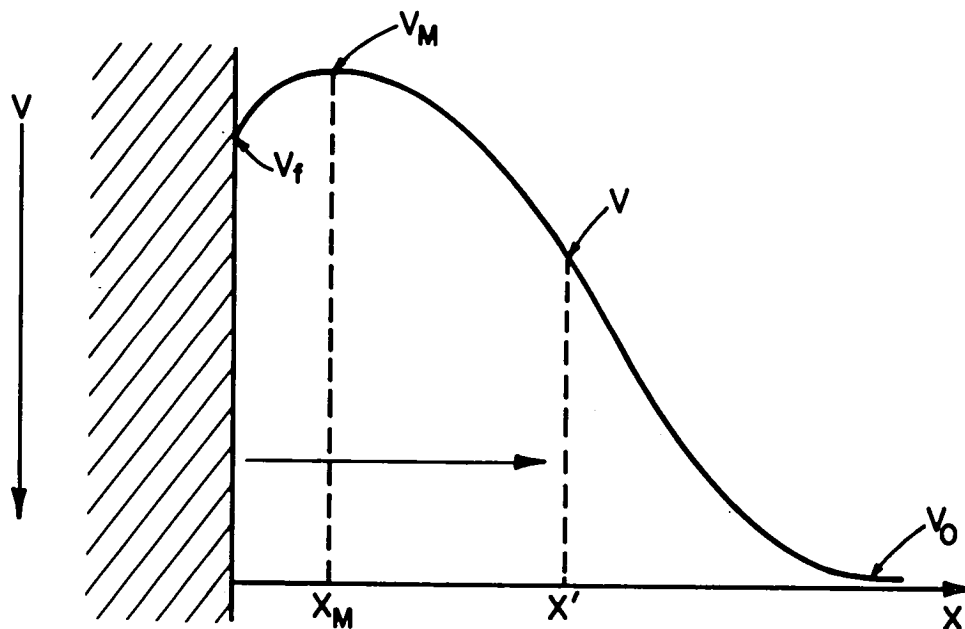
Only those filament electrons with an initial velocity between $\left[\frac{2e}{M_e}(V_f-V_M)\right]^{\frac{1}{2}}$ and ∞ can contribute to the filament electron charge density at x'. This charge density is given by the following expression:

$$\rho_f = \rho_{fM} \int_{\left[\frac{2e}{M_e}(V_f-V_M)\right]^{\frac{1}{2}}}^{\infty} f(v_{of})\, dv_{of} \quad .$$

Where $f(v_{of})$ is the one-dimensional Maxwellian velocity distribution of electrons at the filament surface

$$f(v_{of}) = \left(\frac{M_e}{2\pi kT_f}\right)^{\frac{1}{2}} \exp\left(\frac{-M_e\, v_{of}^2}{2kT_f}\right)$$

and T_f is the filament electron temperature. Using the filament electron energy equation

$$\frac{1}{2} M_e v_{of}^2 = \frac{1}{2} M_e v_f^2 + e(V_f - V)$$

the Maxwellian velocity distribution function at any velocity v_f is:

$$f(v_f) = \left(\frac{M_e}{2\pi kT_f}\right)^{\frac{1}{2}} \exp\left(\frac{-M_e v_f^2}{2kT_f}\right) \exp\left(\frac{-e(V_f - V)}{kT_f}\right) .$$

When $v_{of}^2 = \frac{2e}{M_e}(V_f - V_M)$ the preceeding energy equation gives

$$e(V_f - V_M) = \frac{1}{2} M_e v_f^2 + e(V_f - V)$$

or

$$v_f = \left[\frac{2e}{M_e}(V - V_M)\right]^{\frac{1}{2}} .$$

Substituting these results into the expression for ρ_f gives:

$$\rho_f = \rho_{fM} \left(\frac{M_e}{2\pi kT_f}\right)^{\frac{1}{2}} \exp\left(\frac{-e(V_f - V)}{kT_f}\right) \int_{\left[\frac{2e}{M_e}(V-V_M)\right]^{\frac{1}{2}}}^{\infty} \exp\left(\frac{-M_e v_f^2}{2kT_f}\right) dv_f .$$

If one sets $t = \left(\frac{M_e}{2kT_f}\right)^{\frac{1}{2}} v_f$ and $dv_f = \left(\frac{2kT_f}{M_e}\right)^{\frac{1}{2}} dt$

and notes that $v_f = \left[\frac{2e}{M_e}(V-V_M)\right]^{\frac{1}{2}}$

corresponds to $t = \left[\frac{e}{kT_f}(V-V_M)\right]^{\frac{1}{2}}$

one obtains $\rho_f = \rho_{fM} \left(\frac{M_e}{2\pi kT_f}\right)^{\frac{1}{2}} \exp\left(\frac{-e(V_f - V)}{kT_f}\right) \left(\frac{2kT_f}{M_e}\right)^{\frac{1}{2}} \int_{\left[\frac{e}{kT_f}(V-V_M)\right]^{\frac{1}{2}}}^{\infty} \exp(-t^2) dt$

or

$$\rho_f = \frac{1}{2} \rho_{fM} \exp\left(\frac{-e(V_f-V)}{kT_f}\right)\left[1 - erf\left(\frac{e(V-V_M)}{kT_f}\right)^{\frac{1}{2}}\right] \ .$$

Integrating both sides with respect to V gives

$$\int_{V_M}^{V_o} \rho_f dV = \frac{1}{2} \rho_{fM} \int_{V_M}^{V_o} \exp\left(\frac{e(V-V_f)}{kT_f}\right)\left[1 - erf\left(\frac{e(V-V_M)}{kT_f}\right)^{\frac{1}{2}}\right] dV.$$

Typically, $\left|V_M-V_f\right| \sim T_f \sim 0.2$ eV

and $\left|V\right| \sim$ one volt or more.

Hence, a good approximation is to set $V_f = V_M$.

If one sets $t^2 = \frac{e(V-V_M)}{kT_f}$ then $2tdt = \frac{e}{kT_f} dV$.

When $V = V_m$, $t = 0$, also when $V = V_0$, $t = \left[\frac{e}{kT_f}(V_0-V_M)\right]^{\frac{1}{2}}$.

Substituting these results back into the previous integral gives

$$\int_{V_M}^{V_o} \rho_f dV = \frac{1}{2} \rho_{fM} \int_{V_M}^{V_o} \exp\left(\frac{e(V-V_M)}{kT_f}\right) dV$$

$$- \frac{1}{2} \rho_{fM} \frac{2kT_f}{e} \int_{0}^{\left[\frac{e}{kT_f}V_{OM}\right]^{\frac{1}{2}}} \exp(t^2) \ erf(t) dV$$

where $V_{oM} = V_o-V_M$.

Now for $t^2 \overset{\sim}{>} 5$, in this instance a very good approximation, one can use the following simplification

$$\exp(t^2) \ erf(t) \approx \frac{1}{\pi^{\frac{1}{2}}(t + \frac{1}{2t})} \ .$$

Thus the above integral becomes:

$$\int_{V_M}^{V_o} \rho_f dV = \frac{1}{2} \rho_{fM} \left[\frac{kT_f}{e}\left[\exp\left(\frac{e(V_{oM})}{kT_f}\right) -1\right]\right]$$

$$- \rho_{fM} \frac{2kT_f}{\sqrt{\pi}} e \int_0^{\left(\frac{e}{kT_f} V_{OM}\right)^{1/2}} \frac{t}{t + \frac{1}{2t}} \, dt \quad .$$

But

$$\int \frac{t}{t + \frac{1}{2t}} \, dt = \int \frac{t^2}{\left(\frac{1}{\sqrt{2}}\right)^2 + t^2} \, dt = t - \frac{1}{\sqrt{2}} \arctan(t\sqrt{2})$$

and therefore

$$\int_{V_M}^{V_0} \rho_f dV = \rho_{fM} \left[\frac{kT_f}{2e} \left[\exp\left(\frac{e \, V_{OM}}{kT_f}\right) - 1 \right] - \frac{kT_f}{e\sqrt{\pi}} \left[\frac{e}{kT_f} V_{OM} \right]^{1/2} \right.$$

$$\left. + \frac{kT_f}{e(2\pi)^{1/2}} \arctan \left[\frac{2e}{kT_f} V_{OM} \right]^{1/2} \right] . \tag{B-5}$$

Substituting Eqs. (B-3), (B-4) and (B-5) into (B-1) and remembering that ρ_e and ρ_{fM} are negative, gives:

$$\frac{kT_M}{e} \rho_{oi} \left[\left[1 + \frac{2e}{kT_M} V_{OM} \right]^{1/2} - 1 \right] = \rho_{fM} \left[\frac{kT_f}{2e} \exp\left(\frac{e \, V_{OM}}{kT_f}\right) - 1 - \frac{kT_f}{e\pi^{1/2}} \left[\frac{e}{kT_f} V_{OM} \right]^{1/2} \right.$$

$$+ \frac{kT_f}{e(2\pi)^{1/2}} \arctan \left[\frac{2e}{kT_f} V_{OM} \right]^{1/2} \right] + \frac{1}{12} \rho_{oe} V_{OM} \left[\exp\left(\frac{-e \, V_{OM}}{kT_M}\right) \right.$$

$$\left. + 1 + erf\left(\frac{e \, V_{OM}}{kT_M}\right)^{1/2} + 4 \exp\left(\frac{-e \, V_{OM}}{2kT_M}\right) \left[1 + erf\left(\frac{e \, V_{OM}}{2kT_M}\right)^{1/2} \right] \right] . \tag{B-6}$$

Now Eq. (B-2) had the following form

$$\rho_{fM} V_{fM} + \rho_{iM} V_{iM} = \rho_{eM} V_{eM} \quad .$$

From the previously calculated charge density expressions and initial velocity assumptions each term in this equation can now be determined.

$$\rho_{fM} = \rho_{fM}$$

$$v_{fM} = \left[\frac{8kT_f}{\pi M_e} + \frac{2e}{M_e}(V_M - V_f)\right]^{\frac{1}{2}}$$

$$\rho_{iM} = \rho_{oi}\left[1 + \frac{2e}{kT_M}V_{OM}\right]^{-\frac{1}{2}}$$

$$v_{iM} = \left[\frac{kT_M}{M_i} + \frac{2e}{M_i}V_{OM}\right]^{\frac{1}{2}}$$

$$\rho_{eM} = \frac{1}{2}\rho_{oe}\exp\frac{-eV_{OM}}{kT_M}$$

$$v_{eM} = \left[\frac{8kT_M}{\pi M_e} - \frac{2e}{M_e}V_{OM}\right]^{\frac{1}{2}} \quad .$$

Substituting back into Eq. (B-2) and dividing by ρ_{fM} gives:

$$\left[\frac{8kT_f}{\pi M_e} + \frac{2e}{M_e}(V_M - V_f)\right]^{\frac{1}{2}} + \frac{\rho_{oi}}{\rho_{fM}}\left[\frac{\frac{kT_M}{M_i} + \frac{2e}{M_i}V_{OM}}{1 + \frac{2e}{kT_M}V_{OM}}\right]^{\frac{1}{2}}$$

$$= \frac{1}{2}\frac{\rho_{oe}}{\rho_{fM}}\exp\left(\frac{-eV_{OM}}{kT_M}\right)\left[\frac{8kT_M}{\pi M_e} - \frac{2e}{M_e}V_{OM}\right]^{\frac{1}{2}}$$

or

$$\frac{\rho_{oi}}{\rho_{fM}} = \frac{\left[\frac{1}{2}\frac{\rho_{oe}}{\rho_{fM}}\exp\left(\frac{-eV_{OM}}{kT_M}\right)\left[\frac{8kT_M}{\pi M_e} - \frac{2e}{M_e}V_{OM}\right]^{\frac{1}{2}} - \left[\frac{8kT_f}{\pi M_e} + \frac{2e}{M_e}(V_M-V_f)\right]^{\frac{1}{2}}\right]}{\left[\frac{\frac{kT_M}{M_i} + \frac{2e}{M_i}V_{OM}}{1 + \frac{2e}{kT_M}V_{OM}}\right]^{\frac{1}{2}}}$$

Dividing both sides of Eq. (B-6) by ρ_{fM} and substituting in the above expression for $\frac{\rho_{oi}}{\rho_{fM}}$ yields, after re-arrangement, the following equation:

$$\frac{\dfrac{kT_M}{e}\left[\left[1+\dfrac{2e}{kT_M}V_{OM}\right]^{\frac{1}{2}}-1\right]\left[\dfrac{1}{2}\dfrac{\rho_{oe}}{\rho_{fM}}\exp\left(\dfrac{-eV_{OM}}{kT_M}\right)\left[\dfrac{8kT_M}{\pi M_e}-\dfrac{2e}{M_e}V_{OM}\right]^{\frac{1}{2}}-\left[\dfrac{8kT_f}{\pi M_e}+\dfrac{2e}{M_e}(V_M-V_f)\right]^{\frac{1}{2}}\right]}{\left[\left(\dfrac{kT_M}{M_i}+\dfrac{2e}{M_i}V_{OM}\right)\Big/\left(1+\dfrac{2e}{kT_M}V_{OM}\right)\right]^{\frac{1}{2}}}$$

$$-\frac{1}{12}\frac{\rho_{oe}}{\rho_{fM}}V_{OM}\left[\exp\left(\frac{-eV_{OM}}{kT_M}\right)+1+\operatorname{erf}\left(\frac{eV_{OM}}{kT_M}\right)+4\exp\left(\frac{-eV_{OM}}{2kT_M}\right)\left[1+\operatorname{erf}\left(\frac{eV_{OM}}{2kT_M}\right)^{\frac{1}{2}}\right]\right]$$

$$=\frac{kT_f}{2e}\left[\exp\left(\frac{eV_{OM}}{kT_f}\right)-1\right]-\frac{kT_f}{e\pi^{\frac{1}{2}}}\left[\frac{e}{kT_f}V_{OM}\right]^{\frac{1}{2}}+\frac{kT_f}{e(2\pi)^{\frac{1}{2}}}\arctan\left[\frac{2e}{kT_f}V_{OM}\right]^{\frac{1}{2}}\quad.\quad\text{(B-7)}$$

Standard operating conditions of the ion source used in the screen hole plasma sheath study resulted in a Maxwellian electron temperature of $T_M = 8$ eV (92752°K). While the probe filament electron temperature was approximately $T_f = 0.2$ eV (2319°K). Substituting these results in the above equation gives:

$$8\left[\left[1+0.25\,V_{OM}\right]^{\frac{1}{2}}-1\right]\left[0.5\frac{\rho_{oe}}{\rho_{fM}}\exp\left(-0.125\,V_{OM}\right)\left[3.582\times10^{12}-3.516\times10^{11}V_{OM}\right]^{\frac{1}{2}}\right.$$
$$\left.-1.386\times10^5\right]\left[\frac{1.916\times10^7+4.790\times10^6V_{OM}}{1+0.25\,V_{OM}}\right]^{-\frac{1}{2}}$$

$$-\frac{1}{12}\frac{\rho_{oe}}{\rho_{fM}}V_{OM}\left[\exp(-0.125\,V_{OM})+1+\operatorname{erf}(0.125\,V_{OM})+4\exp(-0.0625\,V_{OM})\right.$$
$$\left.[1+\operatorname{erf}(0.0625\,V_{OM})^{\frac{1}{2}}]\right]$$

$$=0.1[\exp(5V_{OM})-1]-0.113[5V_{OM}]^{\frac{1}{2}}+0.080\arctan[10V_{OM}]^{\frac{1}{2}}\quad.\qquad\text{(B-8)}$$

Solutions to Eq. (B-7) were sought for different $\dfrac{\rho_{oe}}{\rho_{fM}}$ values. The results are tabulated below.

Table B-1   Double Sheath Potential

$\dfrac{\rho_{oe}}{\rho_{fM}}$	V_{OM} ~ volts
0.18	0.6
1.0	1.5
10	2.0
100	2.5
1000	3.0
10000	3.45
100000	3.92

No solutions were possible for $\dfrac{\rho_{oe}}{\rho_{fM}}$ values below 0.18. The formalism

of Eq. (B-7) seems to suggest that this lack of solution was because a

greater plasma electron current was being requested than the initial

conditions of the problem permitted. With decreasing filament electron

emission (i.e., increasing $\dfrac{\rho_{oe}}{\rho_{fM}}$ values) V_{OM} increases slowly. Since

the model has assumed that there are no primary electrons present, the

cold filament would be expected to float several volts below plasma

potential. This result is born out by the trend in the above table.

The results of the model indicate that if the sheath probe filament

were emitting electrons sufficient to make the ratio $\dfrac{\rho_{oe}}{\rho_{fM}} < 1$ then the

probe potential measurements in the bulk plasma would be in error by

about one volt. Since the plasma electron temperature used in Eq. (B-8)

corresponded to a plasma potential of about 43 volt this means the

screen hole sheath probe error is about 2-3% of the true plasma potential

and on the low side.

Filament Electron Emission

The preceeding model has assumed that more electrons are being produced by the filament than are necessary to maintain zero net current between the filament and bulk plasma. A worse case is to assume that all the filament electrons produced are used to maintain this zero net current requirement. Under these conditions the electrons leave the filament with space charge limited emission. Consequently, no virtual cathode is formed and only a single sheath is present. Hence, ρ_{fM} may be replaced by ρ_{fo} the filament electron charge density at the filament. The filament temperature, under typical operating conditions, has been estimated to be 2750°K. This corresponds to a filament electron temperature of 0.24 eV. Using this temperature and the Richardson-Dushman equation, the charge density of 8 eV plasma electrons to the charge density of filament electrons, $\dfrac{\rho_{oe}}{\rho_{fo}}$, is about 0.1. This result indicates that the emissive probe filament is more than capable of providing the emission levels to keep the magnitude of the double sheath potential hill to acceptably small values.

A flat planar filament has been assumed for the sheath probe error model. In reality, the filament was a thin hairpin of tungsten wire. (Fig. 4a). However, at typical discharge plasma conditions the thickness of the double sheath surrounding the probe filament has been estimated to be at least of the order of the filament wire diameter. Under such conditions, a flat planar filament is a fair approximation to the actual physical situation.

Probe Error in Screen Hole Sheath

When the emissive filament enters the screen hole plasma sheath the double sheath adjacent to the probe changes. The ions are being

accelerated through the screen hole sheath but the ion current to the filament remains constant from the ion flux conservation requirement. Also, the filament heating power and hence temperature remains fixed and consequently the number and energy of filament electrons available for electron emission is unaltered. What does change however, is the filament directed plasma electron current at any point through the sheath. This current decreases with distance through the sheath while the temperature of this plasma electron current remains unchanged. Therefore, one would expect a decreasing filament emission current the farther in the sheath is probed in order to maintain zero net current between the quasi plasma in the sheath and the filament. If the probe were pushed through the sheath so that no significant number of plasma electrons were present, the probe filament would be expected to accumulate a positive charge due to the incident ion flux. This behavior was observed experimentally.

The model developed here has taken no account of the presence of primary electrons in the discharge plasma. This assumption would seem valid because the ratio of primary to Maxwellian plasma electrons is approximately 20% for the discharge plasma under consideration. The importance of primary electrons, as far as the probe error is concerned, is that they are the specie which defines the downstream screen hole sheath boundary. Since the primary electron number density is relatively small those primary electrons which define the sheath boundary contribute a small electron current to the probe which drops off rapidly as the sheath boundary is approached. The definite size of the sheath probe filament precludes adequate resolution of this termination region. This resolution loss becomes significant only when the

sheath has been probed to a depth where the sheath potential has dropped to a value about 40% of the plasma potential. At this point, the potential is decreasing with distance so quickly that two filament widths account for the remaining 40% of plasma potential (Fig. 7).

PLASMA ION SHEATH TRAJECTORIES

It is of interest to know how faithfully plasma ion trajectories follow the electric field lines in the screen hole plasma sheath. These ion trajectories may be determined by considering the following diagram which shows a portion of a typical screen hole plasma sheath.
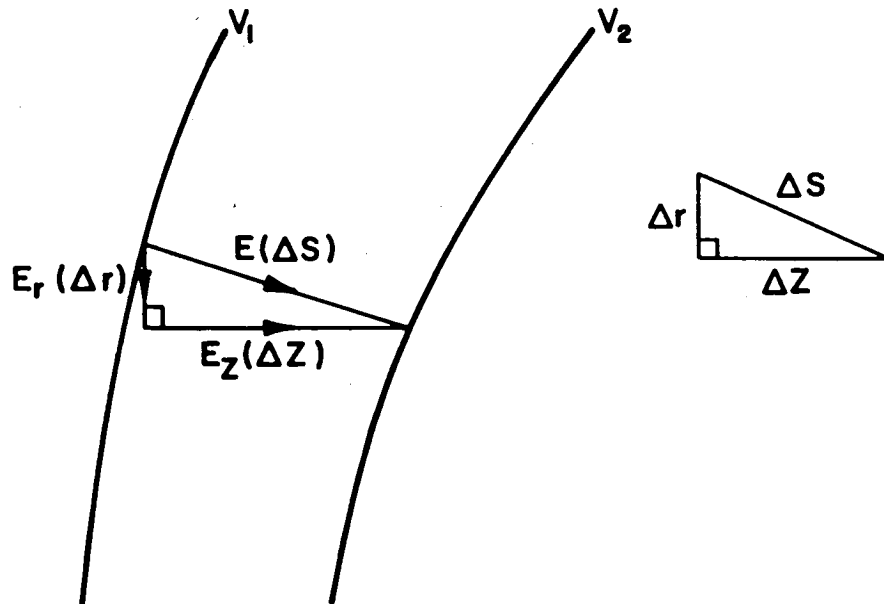
Here, V_1 and V_2 are the magnitudes of any two equipotential contours, $E(\Delta S)$ is the average electric field strength between these contour lines and is a function of their separation ΔS, while $E_r(\Delta r)$ and $E_z(\Delta Z)$ are the radial and axial components respectively of $E(\Delta S)$. The acceleration a plasma ion receives upon passing between V_1 and V_2 has the following components

$$a_r = \frac{E_r(\Delta r)e}{M_i} \tag{C-1}$$

and

$$a_z = \frac{E_z(\Delta Z)e}{M_i} \tag{C-2}$$

where M_i and e are the ion mass and electronic charge respectively. Equations of motion describing ion motion between V_1 and V_2 are given by

$$v_r^2 = v_{or}^2 + 2a_r\Delta r \tag{C-3}$$

and,

$$v_z^2 = v_{oz}^2 + 2a_z\Delta z \quad . \tag{C-4}$$

Where v_r and v_z are the radial and axial ion velocity components at V_2 while v_{or} and v_{oz} are the initial radial and axial velocity components at V_1. Substituting Eqs. (C-1) and (C-2) into Eqs. (C-3) and (C-4) respectively gives

$$v_r^2 = v_{or}^2 + \frac{2e\Delta r \, E_r(\Delta r)}{M_i} \tag{C-5}$$

and,

$$v_z^2 = v_{oz}^2 + \frac{2e\Delta z \, E_z(\Delta z)}{M_i} \quad . \tag{C-6}$$

Equations (C-5) and (C-6) were used to calculate plasma ion trajectories through a typical screen hole plasma sheath profile. Ions were assumed to enter the screen hole plasma sheath at a distance of one screen hole diameter from the origin with the modified Bohm velocity developed by Masek.[16,27] This velocity is given by

$$v = \left[\frac{eT_m}{M_i} \left(1 + \frac{n_p}{n_m}\right) \right]^{\frac{1}{2}}, \tag{C-7}$$

)

where e is the electronic charge and T_m and $\frac{n_p}{n_m}$ are the Maxwellian electron temperature and primary-to-Maxwellian electron density ratio; these parameters were equal to 7.8 eV and 0.20 respectively for the screen hole sheath used in the ion trajectory calculations. Ion trajectories were investigated for initial ion velocities parallel to and 10° above and below the axial co-ordinate direction. In the case of the non-axial initial velocities, the appropriate cosine and sine were multiplied by Eq. (C-7) to define the initial axial and radial velocity components respectively. By calculating the angle between the axial and radial velocity components obtained after each $V_1 \rightarrow V_2$ potential step, the overall ion trajectory through the sheath could be plotted.

Figure (C-1) shows the results of these ion trajectory calculations. Ions entering the sheath parallel to the sheath electric field vector lag behind this vector, but not significantly. Similarly, those ions entering the sheath with the off-axis angles shown are eventually brought into reasonable alignment with the local sheath electric field vector. It should be mentioned that plasma ions assume the modified Bohm velocity as a result of the slight potential gradients which extend back into the center of the ion production region of the discharge chamber. Since plasma ions are created with a randomly directed energy equal to the discharge chamber temperature ($\sim$0.06 eV), they must become aligned rapidly with the bulk plasma electric fields, which although small, can and do accelerate these ions up to a velocity of several eV before they enter the screen hole plasma sheath. Consequently, one would expect most of the ions to enter the sheath parallel to the sheath electric field vector. For an ion to have even a 10° departure from axial

ELECTRIC FIELD VECTOR

CALCULATED ION TRAJECTORIES

CASE A : ION ENTERING SHEATH PARALLEL
TO ELECTRIC FIELD VECTOR

CASE B : ION ENTERING SHEATH 10° ABOVE
ELECTRIC FIELD VECTOR

CASE C : ION ENTERING SHEATH 10° BELOW
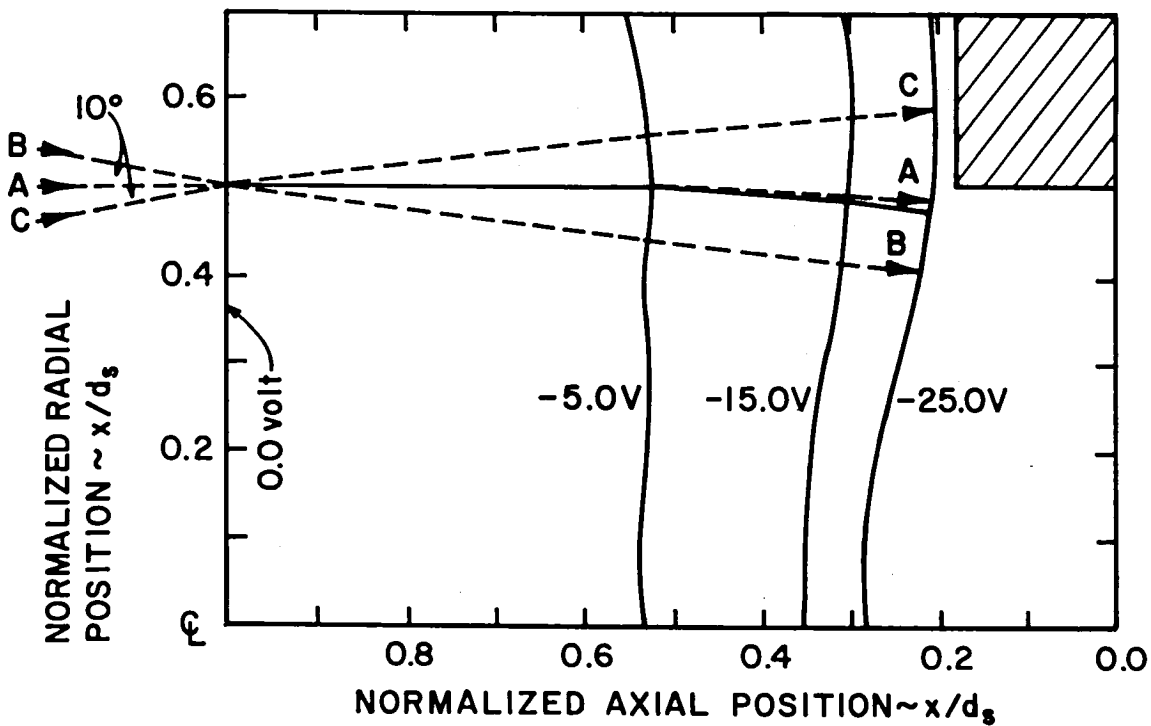ELECTRIC FIELD VECTOR

Fig. C-1 Ion trajectories through a screen hole plasma sheath.

alignment would be unlikely because the ion production rate near the screen grid for the ion source used is small.[22] Also, the probability of ion-neutral atom collisions or charge exchange processes was small because of the low ion source propellant pressures used.

In summary, it may be stated that ion trajectories through the screen hole plasma sheath follow the local sheath electric field vectors to a fair approximation.

APPENDIX D

SHEATH ION AND ELECTRON DENSITY VARIATION

In order to determine the electron and ion number density varia-
tion through the screen hole plasma sheath the three equations follow-
ing were considered:

$$\nabla^2 V = \frac{e(n_e - n_i)}{\varepsilon_0} \quad , \tag{D-1}$$

$$n_i V_i = n_0 \left[\frac{KT_m}{M_i} \left(1 + \frac{n_p}{n_m}\right) \right]^{\frac{1}{2}} , \tag{D-2}$$

$$\frac{1}{2} M_i V_i^2 = \frac{1}{2} M_i \left[\frac{KT_m}{M_i} \left(1 + \frac{n_p}{n_m}\right) \right] - eV . \tag{D-3}$$

Here, Eq. (D-1) is Poisson's equation for electrons and ions where V
is the sheath potential and is negative. Equation (D-2) equates the
ion flux at any point in the sheath to that at the start of the sheath
where the modified Bohm velocity criterion of Masek[16,27] is assumed to
apply. Equation (D-3) equates the ion energy at any point in the
sheath to the ion kinetic energy at the sheath entrance plus that
gained as the ions are accelerated through the sheath. As before, n_e
and n_i are electron and ion number densities at any point in the sheath,
T_m is the Maxwellian electron temperature, $\frac{n_p}{n_m}$ is the primary-to-
Maxwellian electron density ratio and M_i, e, K and ε_0 are the ion mass,
electron charge, Boltzman constant and free space permitivity
respectively.

Azimuthal symmetry is assumed and consequently a one-dimensional
analysis is pursued. In this instance the co-ordinate direction of
interest is perpendicular to the screen hole sheath centerline. With
these assumptions Eq. (D-1) reduces to

$$\frac{\partial^2 V}{\partial z^2} = \frac{e(n_e - n_i)}{\varepsilon_o} \qquad (D-4)$$

Rearranging Eq. (D-3) gives

$$v_i = \left(\left[\frac{KT_m}{M_i} \left(1 + \frac{n_p}{n_m} \right) \right] - \frac{2eV}{M_i} \right)^{\frac{1}{2}} .$$

Substituting this expression back into Eq. (D-2) yields

$$n_i = \frac{n_o \left[\frac{KT_m}{M_i} \left(1 + \frac{n_p}{n_m} \right) \right]^{\frac{1}{2}}}{\left(\left[\frac{KT_m}{M_i} \left(1 + \frac{n_p}{n_m} \right) \right] - \frac{2eV}{M_i} \right)^{\frac{1}{2}}} . \qquad (D-5)$$

This expression may be substituted back into Eq. (D-4) to obtain a relation for n_e that is

$$\frac{\partial^2 V}{\partial Z^2} = \frac{en_e}{\varepsilon_o} - \frac{en_o \left[\frac{KT_m}{M_i} \left(1 + \frac{n_p}{n_m} \right) \right]^{\frac{1}{2}}}{\varepsilon_o \left(\left[\frac{KT_m}{M_i} \left(1 + \frac{n_p}{n_m} \right) \right] - \frac{2eV}{M_i} \right)^{\frac{1}{2}}}$$

or

$$n_e = \frac{\varepsilon_o}{e} \frac{\partial^2 V}{\partial Z^2} + \frac{n_o \left[\frac{KT_m}{M_i} \left(1 + \frac{n_p}{n_m} \right) \right]^{\frac{1}{2}}}{\left(\left[\frac{KT_m}{M_i} \left(1 + \frac{n_p}{n_m} \right) \right] - \frac{2eV}{M_i} \right)^{\frac{1}{2}}} . \qquad (D-6)$$

Equations (D-5) and (D-6) may be solved numerically to find n_i and n_e, since all other parameters can be obtained experimentally.

REFERENCES

1. Coupland, J. R., Green, T. S., Hammond, D. P. and Riviere, A. C., "A Study in the Ion Beam Intensity and Divergence Obtained from a Single Aperture Three Electrode Extraction System," Rev. Sci. Instrum., Vol. 44, No. 9, Sept. 1973, pp. 1258-1270.

2. Alterburg, W., Freisinger, J., Häuser, J., Seibert, N., and Loeb, H. W., "Beam Formation in RF-Ion Thrusters," AIAA Paper No. 75-426, New Orleans, La., 1975.

3. Aston, G. and Kaufman, H. R., "The Ion-Optics of a Two-Grid Electron-Bombardment Thruster," AIAA Paper No. 76-1029, Key Biscayne, Fl., 1976.

4. Kaufman, H. R., "Accelerator System Solutions for Broad Beam Ion Sources," AIAA Journal, Vol. 15, July 1977, pp. 1025-1034.

5. Grisham, L. R., Tsai, C. C., Shealton, J. H. and Stirling, W. L., "Effect of Emission Aperture Shape Upon Ion Optics," Rev. Sci. Instrum., Vol. 48, No. 8, Aug. 1977, pp. 1037-1041.

6. Aston, G., Kaufman, H. R. and Wilbur, P. J., "Ion Beam Divergence Characteristics of Two-Grid Accelerator Systems," AIAA Journal, Vol. 16, No. 5, May 1978, pp. 516-524.

7. Aston, G. and Kaufman, H. R., "Ion Beam Divergence Characteristics of Three-Grid Accelerator Systems," AIAA Journal, Vol. 17, No. 1, Jan. 1979, pp. 64-70.

8. Harrison, E. R., "Investigation of the Perveances and Beam Profiles of an Aperture Disk Emission System," J. Appl. Phys., Vol. 29, No. 6, June 1958, pp. 909-913.

9. Hamza, V. and Richley, E. A., "Numerical Evaluation of Ion-Thruster Optics," NASA TN D-1665, May, 1963.

10. Goldin, D. S. and Cohen, E., "Plasma Extraction Optics Study," TRW Report No. 14176-6001- TO-00, Sept., 1971.

11. Langmuir, I., J. Franklin Inst. 196, 571 (1923). Also in "The Collected Works of Irving Langmuir," edited by C. Guy Suits, Pergamon Press, Inc., New York, 1961, Vol. 5, pp. 1-10.

12. Kemp, R. F. and Sellen, Jr., J. M., "Plasma Potential Measurements by Electron Emissive Probes," Rev. Sci. Instrum., Vol. 37, No. 4, April 1966, pp. 455-461.

13. Martin, A. R., "Electron Energy Distributions in an Ion Engine Discharge," Journal of Space Craft and Rockets, Vol. 8, No. 5, May 1971, pp. 548-550.

14. Beattie, J. R., "Numerical Procedure for Analyzing Langmuir Probe Data," AIAA Journal, Vol. 13, No. 7, July 1975, pp. 950-952.

15. Mott-Smith, H. M. and Langmuir, I., "The Theory of Collectors in Gaseous Discharges," Phys. Rev., Vol. 28, Oct. 1926, pp. 727-763.

16. Bohm, D., "Minimum Ionic Kinetic Energy for a Stable Sheath," in The Characteristics of Electrical Discharges in Magnetic Fields, edited by A. Guthrie and R. K. Wakerling, McGraw-Hill, New York, 1949, pp. 77-86.

17. Fry, T. C., "The Thermionic Current Between Parallel Plane Electrodes; Velocities of Emission Distributed According to Maxwell's Law." Phys. Rev. second series, Vol. 17, No. 4, April 1921, pp. 441-452.

18. Kerrisk, D. J. and Masek, T. D., "Plasma Nonuniformity and Grid Erosion in an Electron Bombardment Ion Engine," AIAA Journal, Vol. 3, No. 6, June 1965, pp. 1060-1066.

19. Hyman, Jr. J., Eckhardt, W. O., Knechtli, R. C. and Buckey, C. R., "Formation of Ion Beams From Plasma Sources: Part 1," AIAA Journal, Vol. 2, No. 10, Oct. 1964, pp. 1739-1748.

20. Kaufman, H. R., Private Communication.

21. Kaufman, H. R., "Technology of Electron-Bombardment Ion Thrusters," Advances in Electronics and Electron Physics, Vol. 36, Academic Press Inc., San Francisco, 1974, p. 303.

22. Beattie, J. R. and Wilbur, P. J., "Cusped Magnetic Field Mercury Ion Thruster," Journal of Space Craft and Rockets, Vol. 14, No. 12, Dec. 1977, pp. 747-755.

23. Kerslake, W. R. and Pawlik, E. V., "Additional Studies of Screen and Accelerator Grids for Electron-Bombardment Ion Thrusters," NASA Tech. Note, D-1411, Aug. 1963.

24. Bogart, C. D. and Richley, E. A., "A Space-Charge-Flow Computer Program," NASA Tech. Note, D-3394, 1966.

25. Whealton, J. H., Jaeger, E. F., and Whitson, J. C., "Optics of Ion Beams of Arbitrary Perveance Extracted from a Plasma," Journal of Computational Physics, Vol. 27, 1978, pp. 1-10.

26. Kaufman, H. R., Harper, J. M. E. and Cuomo, J. J., "Focused Ion Beam Designs for Sputter Deposition," J. Vac. Sci Technol. Vol. 16, No. 3, May/June 1979, pp. 899-905.

27. Masek, T. D., "Plasma Properties and Performance of Mercury Ion Thrusters," AIAA Paper No. 69-256, 1969.

28. Goldan, P. D., "Collisionless Sheath - An Experimental Investigation, "Phys. Fluids, Vol. 13, No. 4, April 1970, pp. 1055-1059.

29. Self, S. A., "Exact Solution of the Collisionless Plasma-Sheath Equation," Phys. Fluids, Vol. 6, No. 12, Dec. 1963.